ISSN 1075-7015, Geology of Ore Deposits, 2007, Vol. 49, No. 1, pp. 31–68. © Pleiades Publishing, Ltd., 2007.
Original Russian Text © V.Yu. Prokof'ev, L.D. Zorina, V.A. Kovalenker, N.N. Akinfiev, I.A. Baksheev, A.N. Krasnov, G.A. Yurgenson, N.V. Trubkin, 2007, published in Geologiya Rudnykh Mestorozhdenii, 2007, Vol. 49, No. 1, pp. 37–76.

Composition, Formation Conditions, and Genesis of the Talatui Gold Deposit, the Eastern Transbaikal Region, Russia

V. Yu. Prokof'ev[a], L. D. Zorina[b], V. A. Kovalenker[a], N. N. Akinfiev[a], I. A. Baksheev[c], A. N. Krasnov[a], G. A. Yurgenson[d], and N. V. Trubkin[a]

[a]*Institute of Geology of Ore Deposits, Petrography, Mineralogy, and Geochemistry, Russian Academy of Sciences, Staromonetnyi per. 35, Moscow, 119017 Russia*

[b]*Vinogradov Institute of Geochemistry, Siberian Division, Russian Academy of Sciences, ul. Favorskogo 1a, Irkutsk, 664033 Russia*

[c]*Faculty of Geology, Moscow State University, Vorob'evy gory, Moscow, 119899 Russia*

[d]*Institute of Natural Resources, Ecology, and Cryology, Siberian Division, Russian Academy of Sciences, ul. Nedorezova 16a, Chita, 672014 Russia*

Received June 19, 2006

Abstract—The mineral composition of the Talatui gold deposit has been studied with modern methods. Previously unknown minerals (ilmenite, siegenite, glaucodot, wittichenite, matildite, hessite, pilsenite, zircon, tremolite, cummingtonite, hercynite, and goethite) have been identified in the ore. A high Re content has been detected in molybdenite. The spatiotemporal separation of Au and Ag is caused by different mineral species of these elements and their diachronous precipitation during the ore-forming process. Gold crystallized along with early mineral assemblages, beginning from virtually pure gold (the fineness is 996). Silver precipitated largely at the end of the process as hessite (Ag_2Te) and matildite ($AgBiS_2$). The temperature of ore deposition varied from 610 to 145°C, the pressure was 3370–110 bar, and the salt concentration ranged from 56.3 to 0.4 wt % NaCl equiv. The heterogeneous state (boiling) of fluid at the early stages has been documented. The chemical and isotopic compositions of the fluid testify to its magmatic nature and the participation of meteoric water at late stages in the ore-forming process. Thermodynamic modeling reproduces the main specific features of ore formation, including separation of Au and Ag. A physicochemical model of the gold mineralization in the Darasun ore district has been proposed. On the basis of several attributes, the Talatui deposit has been referred to the porphyry gold–copper economic type.

DOI: 10.1134/S1075701507010023

INTRODUCTION

The basic problem of the genesis of ore deposits is important for many objects. The nature of the ore-forming fluid and the genesis of the Talatui gold deposit, which has an untypical mineral composition, is discussed in this paper. Despite a number of special features of ores, many researchers have traditionally referred this deposit to the gold–sulfide geological and economic type (Saitov et al., 2002). The mineralogy of ore at this deposit has been studied by specialists of the Darasun Geological Exploration Expedition; the Transbaikal Interdisciplinary Research Institute; Irkutsk Polytechnical Institute; the Institute of Geochemistry, Siberian Division, Russian Academy of Sciences (RAS); the Irkutsk Research Institute of Noble and Rare Metals and Diamonds; the Central Institute of Geological Exploration for Base and Precious Metals; and some other institutions. However, this information is contained largely in open-file reports, and only a few abstracts and two papers (Yurgenson and Yurgenson, 1995; Prokof'ev et al., 2005b) have been published. As judged from the published data, the Talatui deposit differs appreciably from most gold deposits of the Transbaikal region by widespread oxide–sulfide mineral assemblages and Au–Cu–W–Mo specialization of ore. The genetic type of the deposit remains a matter of debate. Therefore, the detailed study of the ore mineralogy, formation conditions of ore, and composition of ore-forming fluid, as well as comparison with other deposits both in this region and worldwide, is of interest. Such study has become especially important at present because mining was begun at the Talatui deposit in 2004. The available literature data are controversial. For example, Benevol'sky (2002) pointed out that gold fineness is as high as 870–975, whereas Yurgenson and Yurgenson (1995) reported lower values (685–925). According to Vorob'ev and Gladush (2000), the Au : Ag ratio of ore is about unity; however, in an open-file report by G.A. Yurgenson and colleagues from 1991 that included analytical results on technological samples up to 300 t in mass, it was indicated that this ratio varies from 0.54 to 1.9. We carried out a detailed investigation of the ore with modern methods using samples collected by specialists of the Institute of

Corresponding author: V.Yu. Prokof'ev. E-mail: vpr@igem.ru

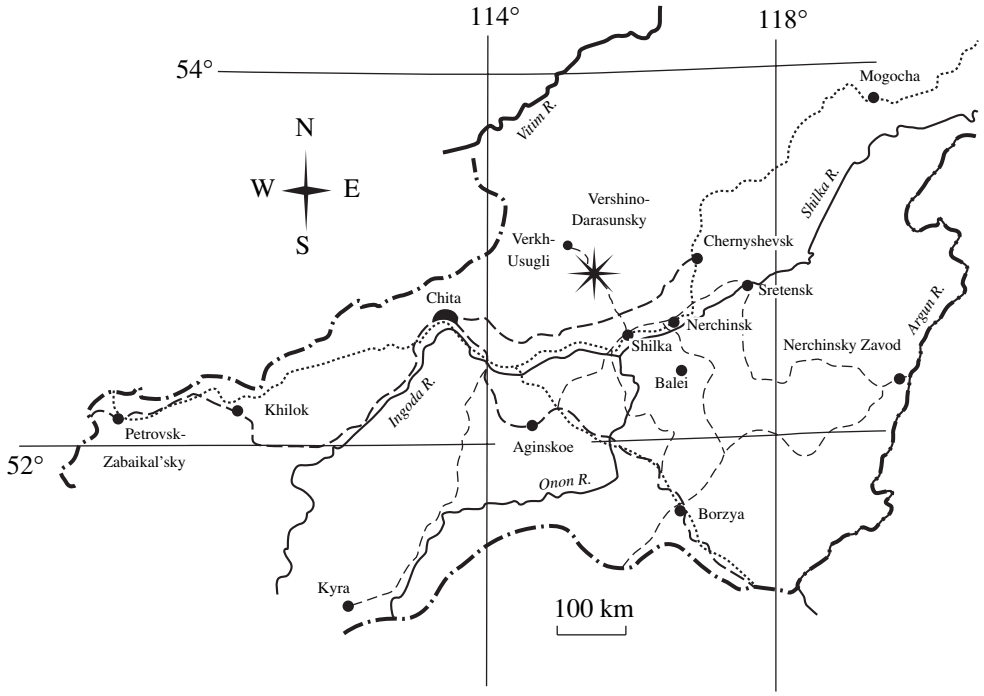

Fig. 1. Index map. The Talatui deposit is indicated by an asterisk that coincides with the settlement of Vershino-Darasunsky on the scale of the map.

Geochemistry, Siberian Division, RAS; the Transbaikal Interdisciplinary Research Institute, Ministry of Geology; and the Institute of Natural Resources, Ecology, and Cryology, Siberian Division, RAS, during geological exploration of this deposit. The results of fieldwork performed by the Institute of Geology of Ore Deposits, Petrography, Mineralogy, and Geochemistry, RAS, in 2001 and 2005 were taken into account as well.

GEOLOGICAL OUTLINE

The Talatui gold deposit is located in Chita oblast (region) 12 km to the northwest of the settlement of Vershino-Darasunsky (Fig. 1) not far from the well-known Darasun gold–sulfide deposit (Fig. 2). The ore is hosted in the hydrothermally altered igneous rocks belonging to the Kruchina Complex of gabbro, gabbro-monzonite, gabbrodiorite, and diorite of Paleozoic age (Fig. 3). The host rocks contact with Triassic granitoids of the Amanan Complex in the northwest and with Late Paleozoic–Early Mesozoic leucogranite, syenite, and granosyenite of the Olekma Complex in the northeast. In the south, they contact with Middle Paleozoic diorite and granodiorite of the Krestovsky Complex. Granitoids are affected by potassic alteration. The host rocks are cut through by Middle–Late Jurassic dikes and stocklike intrusions of porphyritic diorite, granite porphyry, granodiorite porphyry, quartz porphyry, and lamprophyres combined into the Amudzhikan–Sretensk Complex.

The host igneous rocks underwent intense hydrothermal reworking. The examination of thin sections has shown that the host basic rocks are severely altered. The following metasomatic mineral assemblages are predominant: (1) orthoclase, quartz, magnetite, rutile, phlogopite, and tourmaline; (2) epidote, orthoclase, actinolite, phlogopite, pyrite, anhydrite, barite, and quartz; and (3) adularia, chlorite, muscovite (sericite), quartz, and calcite. The zones of hydrothermal alteration make up en echelon arranged system complicated by numerous transverse and longitudinal faults (Il'ina, 1994).

The orebodies are NW-trending vein-shaped and lenticular zones (Fig. 3) 0.25–20 m thick with vague boundaries, which are delineated by results of sampling. These zones are traced for 2000 m along the strike and for 200–500 m down the dip. The ore zones are characterized by the alternation of swells 40–120 m long and pinches reaching 4–20 m in length. The swells are controlled by bends of tectonic zones and transverse faults extending in the northwestern direction. The gold mineralization concentrates in ore shoots at intersections of orebodies with transverse faults.

RESEARCH METHODS

A collection of polished sections prepared from the main ore types was studied with optical ore microscopy followed by analysis of particular minerals on a JSM-5300 SEM equipped with a Link ISIS EDS system at the Institute of Geology of Ore Deposits, Petrog-

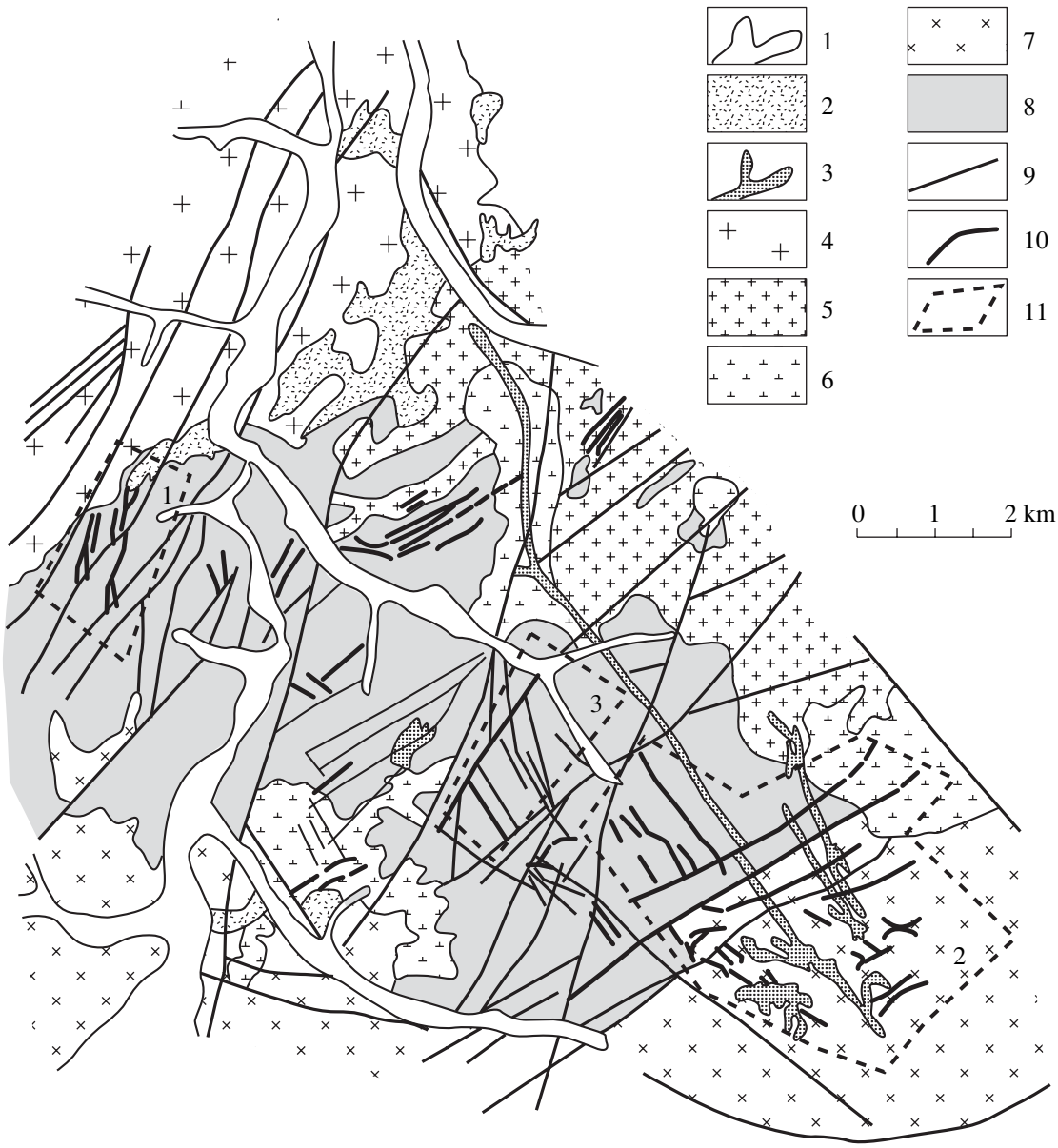

Fig. 2. Geological map of the Darasun ore field, after the data of the Darasun Geological Exploration Expedition. (1) Alluvial sediments; (2, 3) Middle–Late Jurassic Amudzhikan–Sretensk Complex: (2) volcanic rocks, (3) subvolcanic intrusions and dikes: porphyritic diorite, granodiorite and granite porphyries, etc.; (4) Triassic Amanan Complex: biotite–amphibole granite and granodiorite; (5, 6) Late Paleozoic–Early Mesozoic Olekma Complex: (5) biotite granite and leucogranite, (6) syenite, granosyenite, and quartz syenite; (7) Middle Paleozoic Krestovsky Complex: diorite, quartz diorite, and granodiorite; (8) Early Paleozoic Kruchina Complex of metagabbroic rocks: granitized gabbro, amphibolite, gabbrodiorite, and troctolite; (9) faults; (10) orebodies; (11) ore deposits (numerals in map): (1) Talatui, (2) Darasun, (3) Teremki.

raphy, Mineralogy, and Geochemistry, RAS (analyst N.V. Trubkin). The detection limit is 0.4 wt %.

The chemical composition of silicate minerals was determined with a Camebax SX 50 X-ray microprobe at the Department of Mineralogy, Moscow State University (analysts I.A. Bryzgalov and N.N. Kononkova). The current was 30 nA; the accelerating voltage, 15 kV; and the beam diameter, ~3 μm. The measurements were performed according to the following analytical lines: SiK_α, AlK_α, CaK_α, MgK_α, FeK_α, KK_α, NaK_α, FK_α, MnK_α, TiK_α, VK_α, NiK_α, and CrK_α. The detection limit is 0.02 wt %; the measurement uncertainty is ±2% for major elements and ~20% for trace elements. The PAP corrections were used.

The chemical composition of ore minerals was determined on a Camebax SX 100 X-ray microprobe at the Institute of Geochemistry and Analytical Chemistry, RAS (analyst N.N. Kononkova). The current was 30 nA and the accelerating voltage, 20 kV. The measurements were performed according to the following

Fig. 3. Geological sketch map of the Talatui deposit, modified after I.A. Moskovets and A.A. Vorotyntsev (1975). (1–3) Late Jurassic dike complex: (1) porphyritic diorite and microdiorite, (2) fine-grained granite and granite porphyry, (3) granosyenite, monzodiorite, granodiorite, and quartz diorite; (4, 5) Triassic Amanan Complex: (4) medium- and coarse-grained leucogranite, locally porphyritic and biotite-bearing, (5) medium- and coarse-grained, sharply porphyritic amphibole–biotite granodiorite; (6) Early Paleozoic gabbro, gabbrodiorite, and diorite; (7–9) mineralized zones: (7) quartz–tourmaline–sulfide, (8) magnetite–sulfide, (9) sulfide; (10) crush zones; (11) faults; (12) mine and open pit contours.

analytical lines: PbM_α, SK_α, BiM_α, AgL_α, AuL_α, ZnK_α, FeK_α, CdL_α, MnK_α, CuK_α, HgL_α, and SeL_α; the beam diameter was 2–5 μm. The detection limit is 0.02 wt %; the measurement uncertainty is ±2% for major elements and ~20% for trace elements. The PAP corrections were used.

A fire assay for Au and Ag was carried out at the Transbaikal Interdisciplinary Research Institute (analyst V.G. Volkova). Quantitative determinations of Pb and Rb were performed with XRF; W, Cu, and As were determined with AAS at the chemical laboratory of the Transbaikal Interdisciplinary Research Institute (ana-

lysts I.A. Borisova, V.N. Vasil'eva, S.A. Duginets, and O.V. Glushenkova). The chemical analysis of silicate rocks was carried out at the Institute of Geology of Ore Deposits, Petrography, Mineralogy, and Geochemistry, RAS (analyst A.N. Yakushev).

The Moessbauer spectrum of an averaged tourmaline sample was obtained on an SM-2201 spectrometer with ^{57}Co incorporated into a chrome matrix as an irradiation source under a constant acceleration regime at room temperature (analyst A.B. Mironov). The density according to natural iron in samples was ~10 mg/cm^2. The spectrometer was calibrated with a standard sample of sodium nitroprusside. The measurement results were processed with the least-squares method using the SPECTR program in the approximation of a fine absorber (a Lorentzian shape of the line).

Fluid inclusion microthermometry was performed on a measurement complex combining a THMSG-600 microscope heating stage (Linkam, United Kingdom), an Amplival microscope (Germany), a video camera, and a controlling computer. The complex allows one to measure temperatures of phase transition from –196 to 600°C on-line, monitor this process at great magnifications, and take digital photomicrographs. Individual fluid inclusions were studied in plates 0.3–0.5 mm thick polished on both sides. After visual examination and photography, the specimens were unstuck from the glass and washed with ethyl alcohol. Small quartz pieces with inclusions chosen for investigation were then separated mechanically. The salt concentration was calculated from the temperature of either ice melting ($T_{ice\ melt}$) or halite crystal dissolution, after Bodnar and Vityk (1994). The salt composition of solutions was determined from the eutectic temperature (Borisenko, 1977). The pressure of heterogeneous fluid was estimated from substantially gas and gas–liquid syngenetic inclusions as the sum of the partial pressures of water vapor and carbon dioxide. The estimation of salt concentration, as well as water vapor and carbon dioxide pressures, was carried out using the FLINCOR program (Brown, 1989).

Aqueous extracts from inclusions were analyzed by several methods, including gas and ion chromatography and ICP MS, in 0.5-g charges of the 0.50- to 0.25-mm fraction at the Central Institute of Geological Exploration for Base and Precious Metals (analyst Yu.V. Vasyuta); the technique described by Kryazhev et al. (2003) was used. The amount of water in inclusions of the same charge was determined in advance to calculate concentrations of elements in the hydrothermal solution. Carbon dioxide and methane were analyzed as well. After preparation of the extract, Cl, K, Na, Ca, Mg, and all elements that could be detected with ICP MS were determined.

The sulfur isotopic composition of pyrite and chalcopyrite was measured at the Institute of Geology of Ore Deposits, Petrography, Mineralogy, and Geochemistry, RAS (analyst L.P. Nosik). Monomineral samples were selected by hand under a binocular microscope, with a purity of the material no lower than 95%. The measurements were performed on an MI-1311 mass spectrometer. The oxygen isotopic composition of tourmaline was measured at the Institute of Geochemistry and Analytical Chemistry, RAS (analyst V.I. Ustinov) with the fluoride technique of O_2 separation and the subsequent mass spectrometric recording of $\delta^{18}O$ (SMOW) with a reproducibility of ±0.2% (Ustinov, 1983). The $\delta^{18}O$ value was fixed on an MAT-250 gas-phase mass spectrometer that uses O_2 as a working medium. The carbon and oxygen isotopic compositions of carbonates were analyzed at the Central Institute of Geological Exploration for Base and Precious Metals (analyst S.V. Kryazhev) on an MI-1201 mass spectrometer. The salt method was used for decomposition of carbonates (Ustinov and Strizhov, 1976).

CHEMICAL COMPOSITION OF IGNEOUS ROCKS

The host gabbroic rocks are distinguished by elevated contents of alkali metals ($\Sigma K_2O + Na_2O$ = 4–5 wt %), obviously owing to their metasomatic alteration. Granitic rocks comprise plagiogranite with K_2O/Na_2O = 0.25, normal plagioclase–microcline granite with K_2O/Na_2O = 0.7, and a substantially microcline variety with K_2O/Na_2O = 1.9.

The Cr, V, Co, Ni, Cu, Zn, Rb, Sr, Zr, and S contents in gabbroids are variable but broadly fit the global averages for these rocks; B (16–2100 ppm), Cu (29–470 ppm), Rb (48–197 ppm), Zr (up to 304 ppm), and S (0.04–2.13 wt %) are the only exceptions. In plagiogranite, only the Cu and S contents exceed the global average levels (by five times for Cu and by three times for S). In the normal two-feldspar and microcline granites, the contents of all analyzed elements except Zr, V, Zn, and Rb are 1.5–10 times higher than the global averages for these rocks. The excess over this level is especially high for S (5–10 times) and Cu (12–15 times). The Co and Ni contents exceed the global averages by five to eight and two to three times, respectively. Thus, the geochemical specialization of the ore (enrichment in copper up to the formation of massive chalcopyrite ore, as well as the occurrence of Co–Ni mineralization) is probably related to granitic magma.

STRUCTURE OF ORE ZONES

As was mentioned above, the gold mineralization is related to dikes and stocks of Mesozoic granitoids interacting with gabbroids that experienced replacement with biotite, potassium feldspar, tourmaline, quartz, and a propylitic mineral assemblage, as well as superimposed chloritization and carbonation. Tourmalinization and silicification are expressed in both the metasomatic replacement of gabbromonzonite and the development of sulfide–tourmaline–quartz veins and veinlets oriented irregularly or parallel to one another.

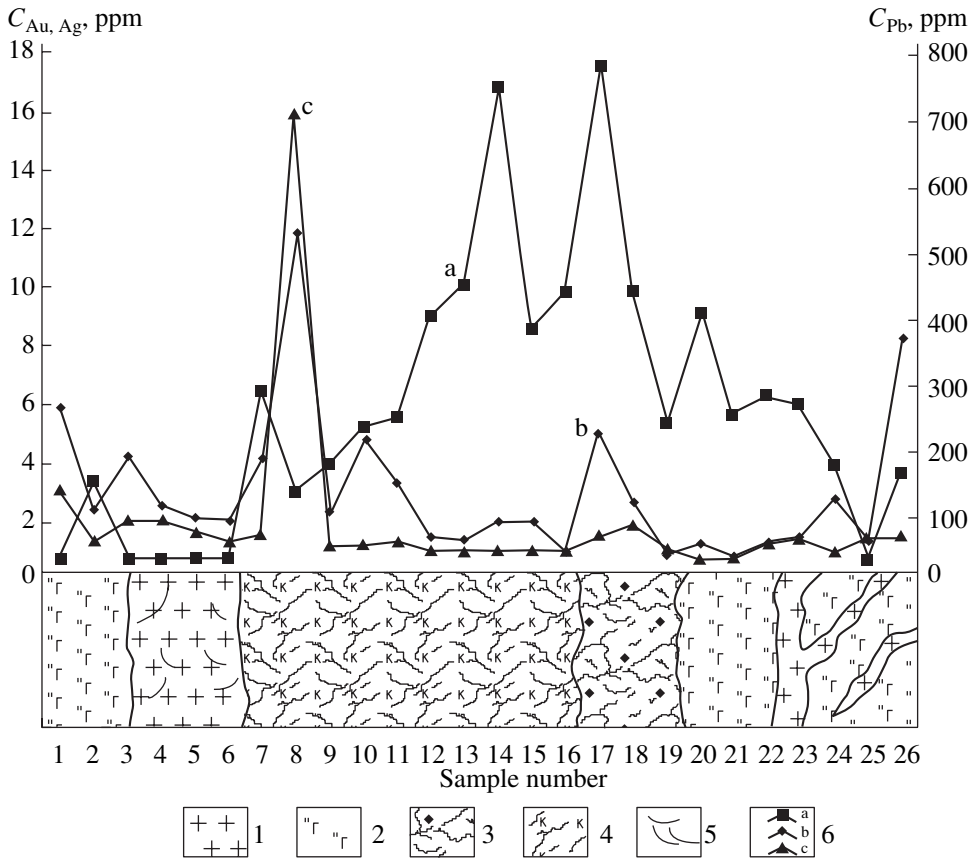

Fig. 4. Au, Ag, and Pb distribution across ore zone 2. (1) Late Jurassic granite and granite porphyry; (2) Early Paleozoic gabbromonzonite and diorite; (3) quartz–sulfide–tourmaline–magnetite assemblage; (4) K-feldspar–quartz–tourmaline–sulfide assemblage; (5) quartz veinlets with sulfides and tourmaline; (6) (a) Au, (b) Ag, and (c) Pb contents.

The thickness of veins does not exceed a few centimeters, and veinlets are a few millimeters thick. As a rule, the veins are not longer than a meter. Quartz–magnetite–sulfide, quartz-tourmaline–sulfide, and sulfide mineral assemblages progressively replace one another up the dip and along the strike from the northwest to the southeast. The vertical zoning in the upper portion of the deposit is probably the same.

Let us consider the structure, mineralogy, petrography, and distribution of major and accompanying ore elements in the sections of ore zones 2 and 3, distinguished in composition and Au grade.

Ore zone 2 was studied at the mine level of 660 m asl (140 m from the surface, drift 1, inset 3, 4 m from its mouth) and in open pit 1 (trenches 8 and 9). At the mine level, the ore zone is 15 m thick, including a 10-m economic portion with an Au grade of 5–17 g/t. Zone 2 is located at the contact of variably altered granitoids with older gabbroic rocks (Fig. 4). The marginal portion of this zone is composed of quartz–feldspar–chlorite–epidote metasomatic rock that contacts with pink fine-grained granite with smoky quartz that often fills small vugs (up to 5 mm across) along with late calcite. Farther inside the ore zone, fine-grained gabbromonzonite locally replaced with granite is intensely feldspathized and cut by quartz–pyrite–chalcopyrite–tourmaline veinlets. This subzone reaches 0.5 m in thickness. The next subzone (4 m) consists of granite. Pink chloritized granite is cut by thin quartz–tourmaline–sulfide veinlets with pyrite and chalcopyrite. Next, a thick (6 m) Au-bearing subzone is composed of metasomatic tourmaline–quartz–K-feldspar rock with pyrite, chalcopyrite, sporadic molybdenite, and chlorite–calcite veinlets. Pyrite also occurs in granite as fine disseminations of small octahedral crystals up to 2–3 mm in size. In the axial portion of this subzone, the pyrite content increases to 10 vol %. This mineral makes up systems of segregations 2–4 cm across. The amount of potassium feldspar diminishes, and the rock becomes three-phase (tourmaline, pyrite, and quartz). In the marginal portion transitional to the magnetite-bearing subzone, chalcopyrite appears again. A pyrite–chalcopyrite–magnetite–tourmaline–quartz subzone, up to 2 m thick, contains visible gold. Next follows a subzone of silicified, sulfide-bearing gabbroids (2 m) cut through by a granitic body; its offsets dissect the slightly altered (epidote, chlorite, and pyrite) gabbroids. The contact of granite with the gabbroids is a boundary of a zone that bears economic ore mineralization.

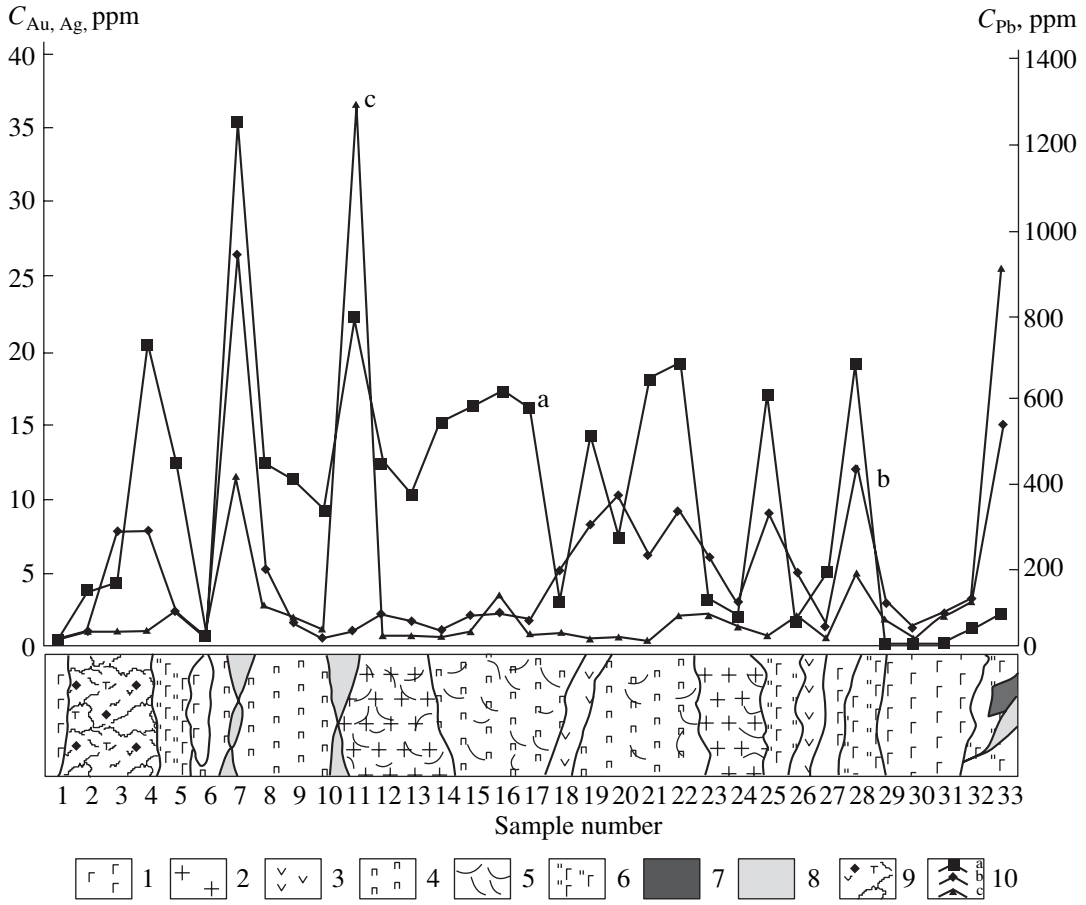

Fig. 5. Au, Ag, and Pb distribution across ore zone 3. (1) Early Paleozoic gabbromonzonite and diorite; (2) Late Jurassic granite and granite porphyry; (3) Late Jurassic microdiorite; (4) propylitic alteration; (5) quartz veinlets with sulfides and tourmaline; (6) feldspathized and silicified gabbroic rocks; (7) potassic alteration within propylites; (8) chlorite–quartz–calcite veins with late sulfides and sulfosalts; (9) quartz–sulfide–tourmaline–magnetite assemblage; (10) (a) Au, (b) Ag, and (c) Pb contents.

In the open pit, ore zone 2 contains Au-bearing massive chalcopyrite ore with pyrite, tourmaline, magnetite, and less abundant quartz as admixtures.

Ore zone 3 observed at the mine level of 660 m (140 m from the surface) in crosscut 2 East is localized in an area of granite–gabbro interaction. The thickness of the pay portion, which mainly corresponds to the quartz–tourmaline–sulfide level of the vertical zoning, is 10–11 m. The zone displays here a rather distinct lateral zoning: the marginal portions are composed of variably altered gabbroic rocks, while the axial portion is occupied by granite, also altered to varying extents.

The following succession of subzones is observable across the strike (Fig. 5). A quartz–sulfide–tourmaline–magnetite subzone up to 2 m thick gives way to silicified, sulfide-bearing gabbro devoid of Au–Ag mineralization. The next propylitic subzone reaches 3 m in thickness and is characterized by economic Au grade. The propylitized gabbro is cut by quartz–chlorite–carbonate veins enriched in galena along with copper and silver sulfosalts. Similar vein systems occur in propylites close to areas of quartz–sulfide veinlets and at contacts with silicified granite, probably responsible for the propylitization. The granite body is 2 m thick. Next follows an Au-bearing subzone of feldspathized propylite, as thick as 4 m, cut by a postmineral microdiorite dike. A similar dike cuts gabbroic rocks at the eastern margin of the ore zone. Another dike-shaped granodiorite body with a low Au content (samples 23–25) occupies the interval at 11–12 m. Granodiorite contacts with feldspathized gabbroic rock that grades into slightly altered rock with a network of quartz–sulfide–tourmaline veinlets (samples 28, 29).

Thus, the highest grade gold mineralization is localized in the subzones with K-feldspar, biotite and phlogopite, tourmaline, a propylitic mineral assemblage, chlorite, and carbonate. The bulk of the early magnetite-bearing productive assemblages are conjugated with potassic alteration, whereas the subsequent pyrite and chalcopyrite generations are related to gold–quartz–tourmaline veinlets. Chalcopyrite veinlets crosscut pyrite–tourmaline–quartz veinlets. As was mentioned above, the chalcopyrite mineralization in ore zone 2 exposed on the surface occurs as massive veinlike bod-

Table 1. Ore minerals at the Talatui deposit

Mineral	Major	Subordinate	Rare
Gangue	Anorthite [$CaAl_2Si_2O_8$]	Actinolite [$Ca_2Fe_5Si_8O_{22}(OH)_2$]	Anhydrite ($CaSO_4$)
	Albite ($NaAlSi_3O_8$)	Tremolite [$Ca_2Mg_5Si_8O_{22}(OH)_2$]*	Barite ($BaSO_4$)
	Quartz(SiO_2)	Cummingtonite [$Mg_7Si_8O_{22}(OH)_2$]*	Apatite [$Ca_5(PO_4)_3F$]
	Orthoclase ($KAlSi_3O_8$)	Epidote $Ca_2FeAl_2Si_2O_{12}OH$	Zircon ($ZrSiO_4$)*
	Tourmaline [$NaFe_3Al_6B_3Si_6O_{27}(OH)_4$]	Titanite ($CaTiSiO_5$)	Chalcedony (SiO_2)
	Sericite [$KAl_3Si_3O_{10}(OH)_2$]	Phlogopite [$KMg_3AlSi_3O_{10}(OH)_2$]	
	Hydromuscovite [$KAl_2Si_4O_{10}(OH)_2$]*	Calcite ($CaCO_3$)	
	Clinochlore [$(Mg, Fe)_5Al_2Si_3(OH)_8$]		
Ore	Pyrite (FeS_2)	Bornite (Cu_5FeS_4)	Molybdenite (MoS_2)
	Chalcopyrite ($CuFeS_2$)	Ilmenite ($FeTiO_3$)*	Glaucodot [(Co, Fe)AsS]*
	Magnetite (Fe_3O_4)	Rutile (TiO_2)	Siegenite ($CoNi_2S_4$)*
	Hematite (Fe_2O_3)	Scheelite ($CaWO_4$)	Pyrrhotite (FeS)
		Goethite (FeOOH)*	Sphalerite (ZnS)
			Galena (PbS)
			Hessite (Ag_2Te)*
			Pilsenite (Bi_4Te_3)*
			Matildite ($AgBiS_2$)*
			Wittichenite (Cu_3BiS_3)*
			Marcasite (FeS_2)
			Gold Au
			Electrum (Au, Ag)
			Wolframite ($FeWO_4$)
			Hercynite ($FeAl_2O_4$)*
			Uraninite (UO_2)

* Minerals identified at the deposit for the first time.

ies 15–40 cm or more in thickness. Silicification and sulfide mineralization become more intense toward the axis of the zone. Close to the margins, the rate of chloritization and the number of carbonate veinlets increase. Galena and Cu and Pb sulfosalts appear in these veinlets together with pyrite, giving rise to elevated Cu and Pb contents. In general, the highest average Pb content is typical of a transition from granite to diorite (Figs. 4, 5).

The Au, Ag, and Pb contents are not correlated throughout the deposit. Such a correlation is only characteristic of quartz–sulfide–tourmaline–magnetite subzones. The bulk of Au ore proper is in quartz–sulfide–tourmaline veinlet systems hosted in metasomatically altered granite and feldspathized hybrid rocks. The late Pb–Ag mineralization is related to carbonate–chlorite–sulfide–sulfosalt veins.

Tungsten (as scheelite) largely concentrates in zones of quartz–sulfide–tourmaline veinlets hosted in metasomatically altered granite and at contacts of quartz–sulfide–tourmaline–magnetite bodies with gabbroic rocks.

The Au and Cu contents are also not correlated. The maximum Cu content is typical of contacts with quartz–sulfide–tourmaline–magnetite subzones and of the later massive chalcopyrite ore. At the same time, Cu is well correlated with Ag. In zones of potassic alteration, Au is correlated with Rb. Additional investigations are required to specify the distribution of chemical elements in orebodies.

ORE COMPOSITION

Gold is the main recoverable component of ore; its average grade is 9.5 g/t (Benevol'sky, 2002). The associated valuable components are as follows (average grades are given in parentheses): Ag (6.4 g/t), Cu (0.16%), W (0.084%), Bi (0.014%), and sulfide sulfur (33%). The results of emission spectrometry of ore samples at the Institute of Geochemistry, Siberian Division, RAS (analyst L.N. Odareeva), and of INAA at the Institute of Geology of Ore Deposits, Petrography, Mineralogy, and Geochemistry, RAS (analyst A.L. Kerzin), yielded the following results (ppm): 170–0.04 Au, 116–0.08 Ag, 1978–185 Cu, 9773–6 W, 142–2 Bi, 1552–16

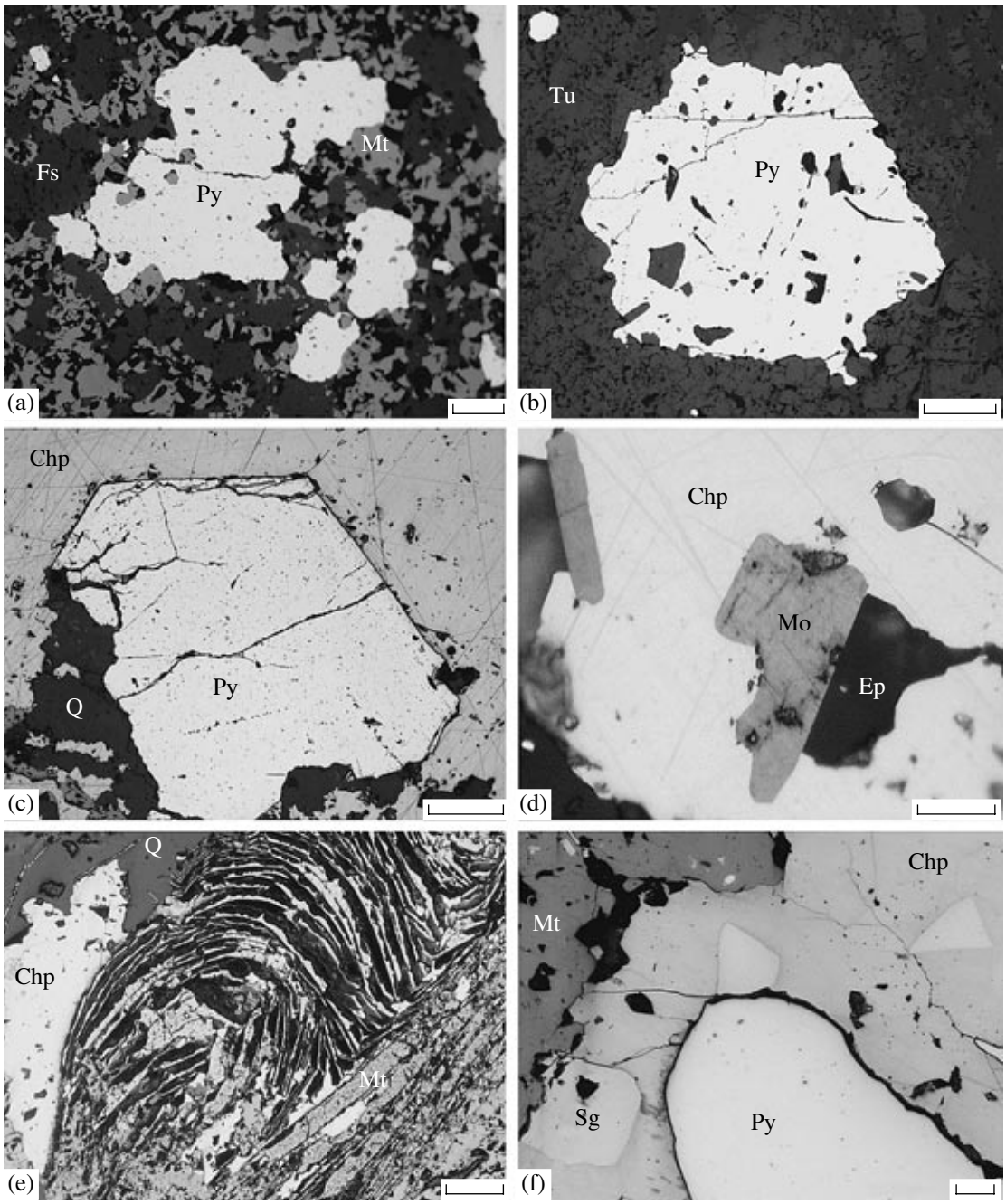

Fig. 6. Main ore mineral assemblages in ore from the Talatui deposit. (a) Pyrite in a feldspar–magnetite aggregate; (b) pyrite in an epidote–tourmaline aggregate; (c) pyrite and quartz in early chalcopyrite; (d) early chalcopyrite and molybdenite and epidote; (e) magnetite pseudomorphs after magnetite, chalcopyrite, and quartz; (f) late chalcopyrite and siegenite at the contact with pyrite and magnetite. (Mt) Magnetite, (Py) pyrite, (Tu) tourmaline, (Fs) feldspar, (Chp) chalcopyrite, (Ep) epidote, (Q) quartz, (Mo) molybdenite, (Sg) siegenite. Scale bar, 100 μm.

As, 54–3 Pb, 1244–14 Zn, 157–2 Mo, 164–23 Ni, 4027–36 Co, 171–56 V, 1106–2.6 Cr, 54 000–10 B, 12–3 Sn, 38–1.1 Sc, 147–12 Se, 13–0.01 Te, 47–0.9 Sb, 6.9–2.0 Cs, 3.1–0.5 Hf, 111.7–0.2 Ta, up to 923 Ba, up to 186 Sr, 1.9–1.5 Tl, 2.2–1.0 Th, and 6.3–0.9 U, as well as 38–1.5 wt % S and 0.97–0.23 wt % TiO_2. The relationships between Au and Ag contents in ore are rather complex. The correlation coefficient in the ore samples taken along the exploration adit is 0.79 (45 samples) for zone 1, 0.52 (96 samples) for zone 2, and 0.32 (62 samples) for zone 3. The low values of the Au–Ag correlation coefficient and the decrease in its values in space may testify to the appearance of Ag minerals and concentration of Ag and Au in different forms. Such a suggestion is the most probable for zone 3, with abundant low-temperature sulfide–sulfosalt chlorite–carbonate mineralization.

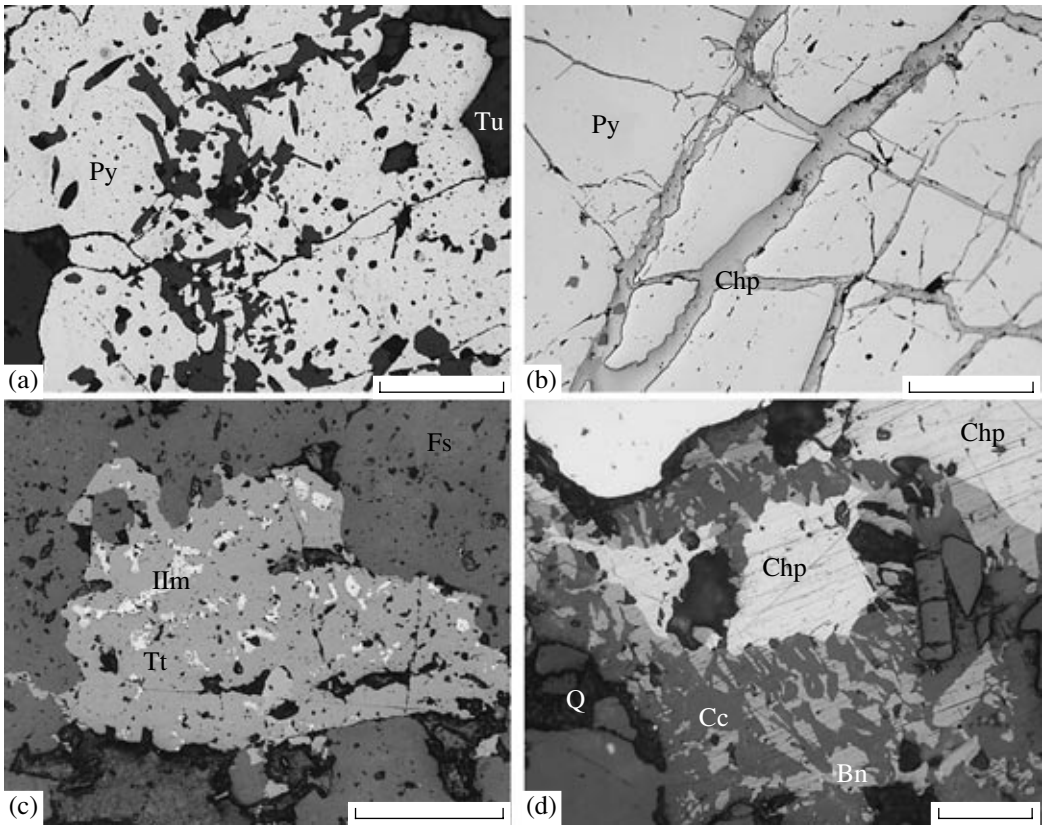

Fig. 7. Relationships between minerals of different assemblages. (a) Euhedral tourmaline crystals in pyrite; (b) veinlets of chalcopyrite in pyrite; (c) ilmenite relics in titanite; (d) chalcopyrite overgrown by a bornite–calcite aggregate. (Py) Pyrite, (Tu) tourmaline, (Chp) chalcopyrite, (Q) quartz, (Ilm) ilmenite, (Tt) titanite, (Bn) bornite, (Cc) calcite. Scale bar, 100 μm.

The modern methods of local microanalysis allowed us to identify a number of mineral phases not described in the literature previously (ilmenite, siegenite, glaucodot, wittichenite, matildite, hessite, pilsenite, zircon, hydromuscovite, tremolite, cummingtonite, hercynite, and goethite). The mineral composition of ore is summarized in Table 1.

As follows from the results of quantitative mineralogical analysis of technological samples (Fig. 6), the following major minerals are contained in ore (wt %): feldspars (15–28); magnetite (19–21); quartz (17–23); pyrite (7–9); chalcopyrite (6–9); and epidote, chlorite, tourmaline, and phlogopite (7–15 in total). Scheelite, sphalerite, titanite, hematite, iron hydroxides (goethite), and hercynite are less abundant. Galena, siegenite, matildite, pilsenite, hessite, wittichenite, anhydrite, barite, wolframite, and zircon, as well as gypsum and pyrrhotite, which forms small inclusions in pyrite and chalcopyrite, are rare. The replacement of magnetite with hematite (martitization) and the formation of magnetite pseudomorphs after platy hematite grains (mushketovitization), typical of ore assemblages, testify to the variation of oxygen fugacity during ore formation. The gangue minerals include feldspars, quartz, epidote, tourmaline, biotite, phlogopite, muscovite (sericite), actinolite, tremolite, clinochlore, chalcedony, and carbonates.

The mutual relationships of minerals (Fig. 7) indicate the following sequence of their formation (Fig. 8). Anorthite, cummingtonite, hercynite, and ilmenite likely are relict minerals of the host gabbroids and are replaced by ore minerals. Orthoclase and magnetite, often in association with pyrite, wolframite, scheelite, epidote, actinolite, tremolite, phlogopite, tourmaline, rutile, quartz, and a small amount of native gold of high fineness with a reddish hue in reflected light, are the earliest minerals. Pyrite, hematite, potassium feldspar, muscovite, titanite, tourmaline, barite, anhydrite in association with native gold of high fineness (also reddish in quartz, epidote, and tourmaline and yellow in pyrite), the early chalcopyrite, and molybdenite were formed later. Fracturing was accompanied by formation of chalcopyrite in association with pyrrhotite, sphalerite, siegenite, glaucodot, muscovite (sericite), quartz, chlorite, and straw-colored gold of a lower fineness. Bismuth and silver minerals (matildite, hessite, pilsenite, wittichenite, etc.) crystallized afterward along with quartz, hydromuscovite, and carbonate. The late sulfide assemblages are characterized by overgrowth of chalcopyrite by bornite (occasionally by pyrite) and by precipitation of carbonates, chalcedony, and rare gypsum and uraninite.

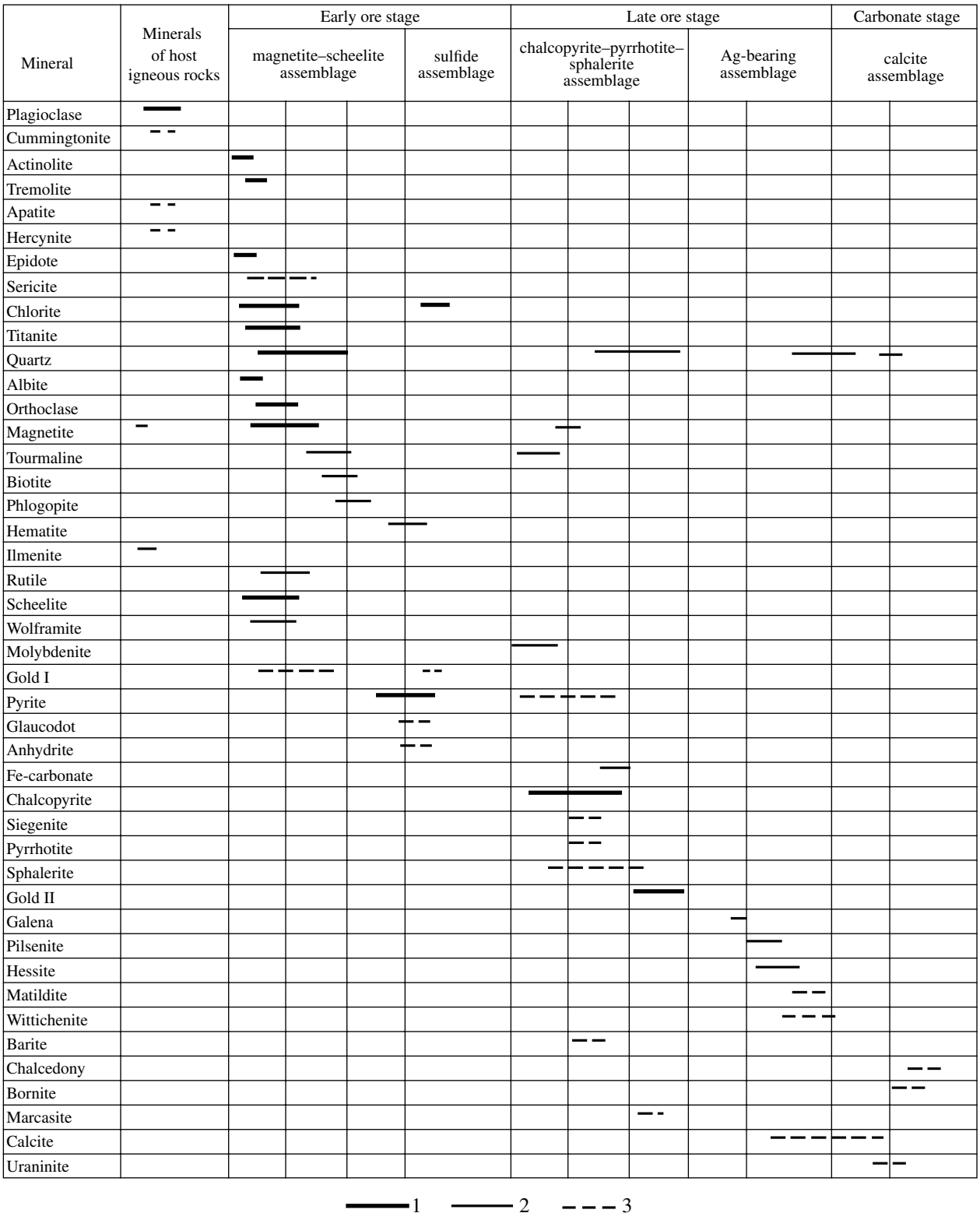

Fig. 8. Sequence of mineral formation in ore at the Talatui deposit. (1) Major, (2) subordinate, and (3) rare minerals.

TYPOMORPHISM OF MINERALS

The local chemical analysis of minerals with an X-ray microprobe allowed us to reveal their specific typomorphic features.

Tourmaline occurs as slightly zonal crystals varying from a few micrometers to a few millimeters in length with pleochroism from light to dark green. Tourmaline inclusions in pyrite and chalcopyrite are frequent. Tour-

Table 2. Chemical composition of tourmaline from the Talatui deposit, wt %

Component	1	2	3	4m	5m	6m	7c	8	9m	10m
B_2O_3	10.39	10.31	10.34	10.17	10.29	10.12	10.59	10.30	10.56	10.62
SiO_2	35.69	35.59	36.20	34.47	36.04	34.60	36.10	35.54	35.82	37.00
TiO_2	0.31	0.00	0.34	0.02	0.02	0.00	0.16	0.84	1.24	0.66
Cr_2O_3	0.19	0.14	0.12	0.14	0.00	0.00	0.02	0.05	0.72	0.00
Al_2O_3	25.97	24.42	26.58	24.64	24.79	20.70	28.47	23.67	27.98	27.83
V_2O_3	0.09	0.10	0.02	0.10	0.00	0.11	0.05	0.10	0.06	0.05
CuO	0.00	0.00	0.09	0.02	0.00	0.05	0.00	0.00	0.00	0.06
FeO_{tot}	15.47	16.56	13.87	16.28	15.64	21.67	11.69	16.52	9.84	11.12
MnO	0.00	0.10	0.04	0.00	0.08	0.05	0.04	0.02	0.00	0.00
MgO	6.73	7.09	6.50	7.01	6.98	6.77	7.89	7.51	8.47	8.03
CaO	2.21	1.78	1.88	1.84	1.89	2.29	0.60	1.15	0.36	1.06
K_2O	0.04	0.04	0.02	0.05	0.02	0.05	0.04	0.06	0.05	0.05
Na_2O	1.60	1.92	1.77	1.93	1.84	1.56	2.62	2.37	2.77	2.24
F	0.12	0.16	0.07	0.00	0.00	0.02	0.22	0.00	0.18	0.00
H_2O	3.02	3.20	2.86	3.27	3.10	3.48	3.31	3.31	3.27	3.21
2F=O	0.05	0.07	0.03	0.00	0.00	0.01	0.09	0.00	0.08	0.00
Total	101.78	101.34	100.67	99.94	100.69	101.46	101.71	101.44	101.24	101.93
Formula units calculated to 15 cations										
B	3.000	3.000	3.000	3.000	3.000	3.000	3.000	3.000	3.000	3.000
Si	5.966	5.995	6.081	5.890	6.086	5.939	5.924	5.995	5.891	6.054
^{T}Al	0.034	0.005	0.000	0.110	0.000	0.061	0.076	0.005	0.109	0.000
Total *T*	6.000	6.000	6.081	6.000	6.086	6.000	6.000	6.000	6.000	6.054
^{Z}Al	5.084	4.783	5.263	4.853	4.934	4.128	5.430	4.702	5.315	5.367
Fe^{2+}	1.081	1.166	0.974	1.163	1.104	1.555	0.802	1.140	0.677	0.761
Fe^{3+}	1.081	1.166	0.974	1.163	1.104	1.555	0.802	1.140	0.677	0.761
Mg	1.677	1.778	1.628	1.786	1.757	1.733	1.930	1.889	2.077	1.959
V	0.012	0.014	0.003	0.014	0.000	0.015	0.007	0.014	0.008	0.007
Ti	0.039	0.000	0.043	0.003	0.003	0.000	0.021	0.107	0.153	0.081
Cr	0.025	0.019	0.016	0.019	0.000	0.000	0.003	0.007	0.094	0.000
Mn	0.000	0.014	0.006	0.000	0.011	0.007	0.006	0.003	0.000	0.003
Cu	0.000	0.000	0.011	0.000	0.000	0.006	0.000	0.000	0.000	0.007
Total ($Y + Z$)	8.999	8.940	8.918	9.001	8.913	8.999	9.001	9.002	9.001	8.946
Na	0.519	0.627	0.577	0.639	0.602	0.519	0.834	0.775	0.883	0.711
Ca	0.396	0.321	0.338	0.337	0.342	0.421	0.105	0.208	0.063	0.186
Vacancy	0.076	0.043	0.081	0.013	0.052	0.049	0.053	0.004	0.044	0.093
K	0.009	0.009	0.004	0.011	0.004	0.011	0.008	0.013	0.010	0.010
Total *X*	1.000	1.000	1.000	1.000	1.000	1.000	1.000	1.000	1.000	1.000
^{V}OH	3.000	3.000	3.000	3.000	3.000	3.000	3.000	3.000	3.000	3.000
^{V}O	0.000	0.000	0.000	0.000	0.000	0.000	0.000	0.000	0.000	0.000
Total *V*	3.000	3.000	3.000	3.000	3.000	3.000	3.000	3.000	3.000	3.000
^{W}O	0.561	0.315	0.759	0.271	0.504	0.004	0.262	0.277	0.312	0.498
^{W}OH	0.376	0.600	0.204	0.729	0.496	0.985	0.624	0.723	0.594	0.502
F	0.063	0.085	0.037	0.000	0.000	0.011	0.114	0.000	0.094	0.000
Total *W*	1.000	1.000	1.000	1.000	1.000	1.000	1.000	1.000	1.000	1.000
f	0.56	0.57	0.54	0.57	0.56	0.64	0.45	0.55	0.39	0.44
Ca/(Ca + Na)	0.43	0.34	0.37	0.35	0.36	0.45	0.11	0.21	0.07	0.21

Table 2. (Contd.)

Component	11c	12	13m	14c	15	16c	17	18m	19c
B_2O_3	10.15	9.92	10.09	9.84	10.23	10.53	10.46	10.35	10.44
SiO_2	34.18	32.89	33.54	33.01	34.45	35.67	34.91	33.82	34.19
TiO_2	0.21	0.10	0.06	0.21	0.29	0.22	0.25	0.80	0.51
Cr_2O_3	0.47	0.31	0.09	0.48	0.00	0.04	0.00	0.00	0.06
Al_2O_3	25.33	26.81	27.14	24.07	26.03	29.10	28.97	27.31	28.82
V_2O_3	0.09	0.00	0.00	0.02	0.06	0.04	0.02	0.00	0.08
CuO	0.10	0.00	0.05	0.00	0.00	0.00	0.00	0.00	0.00
FeO_{tot}	20.58	20.86	18.33	23.40	14.98	11.04	10.78	13.46	11.45
MnO	0.12	0.00	0.03	0.13	0.046	0.00	0.04	0.05	0.03
MgO	3.82	2.26	4.08	2.23	6.93	7.69	8.02	7.66	7.98
CaO	1.49	1.14	1.47	1.38	0.63	0.52	0.59	1.03	0.72
K_2O	0.05	0.05	0.04	0.07	0.05	0.00	0.03	0.03	0.02
Na_2O	1.93	2.06	2.11	1.86	2.46	2.54	2.57	2.28	2.48
F	0.37	0.11	0.09	0.07	0.00	0.07	0.00	0.00	0.07
H_2O	2.83	2.69	2.96	2.77	3.43	3.37	3.48	3.54	3.53
2F=O	0.16	0.05	0.04	0.03	0.00	0.03	0.00	0.00	0.03
Total	101.56	99.15	100.04	99.51	99.59	100.80	100.12	100.33	100.35
Formula units calculated to 15 cations									
B	3.000	3.000	3.000	3.000	3.000	3.000	3.000	3.000	3.000
Si	5.850	5.762	5.775	5.829	5.852	5.886	5.801	5.679	5.689
^{T}Al	0.150	0.238	0.225	0.171	0.148	0.114	0.199	0.321	0.311
Total *T*	6.000	6.000	6.000	6.000	6.000	6.000	6.000	6.000	6.000
^{Z}Al	4.960	5.297	5.282	4.840	5.064	5.547	5.475	5.084	5.341
Fe^{2+}	1.473	1.528	1.320	1.728	1.064	0.762	0.749	0.945	0.797
Fe^{3+}	1.473	1.528	1.320	1.728	1.064	0.762	0.749	0.945	0.797
Mg	0.975	0.590	1.047	0.587	1.755	1.892	1.987	1.918	1.979
V	0.000	0.000	0.000	0.003	0.008	0.005	0.003	0.000	0.011
Ti	0.041	0.013	0.008	0.028	0.037	0.027	0.031	0.101	0.064
Cr	0.000	0.043	0.012	0.067	0.000	0.005	0.000	0.000	0.008
Mn	0.017	0.000	0.004	0.019	0.007	0.000	0.006	0.007	0.004
Cu	0.061	0.000	0.007	0.000	0.000	0.000	0.000	0.000	0.000
Total ($Y + Z$)	9.000	8.999	9.000	9.000	8.999	9.000	9.000	9.000	9.001
Na	0.641	0.700	0.704	0.637	0.810	0.813	0.828	0.742	0.800
Ca	0.273	0.214	0.266	0.261	0.115	0.092	0.105	0.185	0.128
Vacancy	0.075	0.075	0.021	0.086	0.064	0.095	0.061	0.067	0.068
K	0.011	0.011	0.009	0.016	0.011	0.000	0.006	0.006	0.004
Total *X*	1.000	1.000	1.000	1.000	1.000	1.000	1.000	1.000	1.000
^{V}OH	3.000	3.000	3.000	3.000	3.000	3.000	3.000	3.000	3.000
^{V}O	0.000	0.000	0.000	0.000	0.000	0.000	0.000	0.000	0.000
Total *V*	3.000	3.000	3.000	3.000	3.000	3.000	3.000	3.000	3.000
^{W}O	0.563	0.796	0.653	0.695	0.111	0.253	0.134	0.028	0.036
^{W}OH	0.237	0.143	0.298	0.266	0.889	0.710	0.866	0.972	0.927
F	0.200	0.061	0.049	0.039	0.000	0.037	0.000	0.000	0.037
Total *W*	1.000	1.000	1.000	1.000	1.000	1.000	1.000	1.000	1.000
f	0.75	0.84	0.72	0.85	0.55	0.45	0.43	0.50	0.45
Ca/(Ca + Na)	0.30	0.23	0.27	0.29	0.12	0.10	0.11	0.20	0.14

Table 2. (Contd.)

Component	20	21c	22m	23c	24m	25c	26	27
B_2O_3	10.36	10.22	10.67	10.47	10.59	10.61	10.42	10.33
SiO_2	34.68	32.98	35.85	34.85	34.58	35.72	36.42	35.43
TiO_2	0.23	0.23	1.00	0.31	0.19	0.42	0.20	0.70
Cr_2O_3	0.00	0.07	0.00	0.00	0.06	0.00	0.02	0.08
Al_2O_3	27.24	26.80	29.33	28.66	32.91	28.68	28.04	27.46
V_2O_3	0.07	0.05	0.00	0.00	0.00	0.03	0.00	0.00
CuO	0.00	0.00	0.00	0.00	0.03	0.00	0.26	0.00
FeO_{tot}	13.47	15.50	10.04	12.94	7.82	11.63	12.37	11.13
MnO	0.02	0.06	0.08	0.00	0.00	0.00	0.02	0.00
MgO	7.46	6.94	8.40	7.19	7.61	8.07	6.50	7.64
CaO	0.69	0.63	0.21	0.59	0.04	0.60	1.69	1.17
K_2O	0.04	0.04	0.03	0.05	0.06	0.04	0.03	0.04
Na_2O	2.46	2.48	2.87	2.44	2.52	2.51	2.19	2.38
F	0.00	0.00	0.07	0.00	0.23	0.24	0.05	0.14
H_2O	3.49	3.49	3.45	3.47	3.43	3.42	2.55	2.77
2F=O	0.00	0.00	0.03	0.00	0.10	0.10	0.02	0.06
Total	100.21	99.49	101.97	100.97	99.97	101.87	100.79	99.30
Formula units calculated to 15 cations								
B	3.000	3.000	3.000	3.000	3.000	3.000	3.000	3.000
Si	5.817	5.609	5.627	5.782	5.671	5.848	6.075	5.961
^{T}Al	0.183	0.391	0.165	0.218	0.329	0.152	0.000	0.039
Total *T*	6.000	6.000	6.000	6.000	6.000	6.000	6.075	6.000
^{Z}Al	5.203	4.981	5.462	5.387	6.032	5.382	5.513	5.406
Fe^{2+}	0.945	0.882	0.683	0.898	0.536	0.796	0.552	0.501
Fe^{3+}	0.945	1.322	0.683	0.898	0.536	0.796	1.174	1.065
Mg	1.866	1.760	2.038	1.779	1.861	1.970	1.616	1.916
V	0.009	0.007	0.000	0.000	0.000	0.004	0.000	0.00
Ti	0.029	0.029	0.122	0.039	0.023	0.052	0.025	0.089
Cr	0.000	0.009	0.000	0.000	0.008	0.000	0.003	0.011
Mn	0.003	0.009	0.011	0.000	0.000	0.000	0.003	0.000
Cu	0.000	0.000	0.000	0.000	0.000	0.000	0.033	0.000
Total (*Y* + *Z*)	9.000	8.999	8.999	9.001	8.996	9.001	8.919	8.988
Na	0.800	0.818	0.906	0.785	0.801	0.797	0.708	0.776
Ca	0.124	0.115	0.037	0.105	0.007	0.105	0.302	0.211
Vacancy	0.067	0.058	0.051	0.099	0.179	0.090	0.000	0.004
K	0.009	0.009	0.006	0.011	0.013	0.008	0.006	0.009
Total *X*	1.000	1.000	1.000	1.000	1.000	1.000	1.016	1.000
^{V}OH	3.000	3.000	3.000	3.000	3.000	3.000	2.830	3.000
^{V}O	0.000	0.000	0.000	0.000	0.000	0.000	0.170	0.000
Total *V*	3.000	3.000	3.000	3.000	3.000	3.000	3.000	3.000
^{W}O	0.089	0.041	0.208	0.153	0.121	0.137	0.974	0.812
^{W}OH	0.911	0.959	0.756	0.847	0.760	0.739	0.000	0.114
F	0.000	0.000	0.036	0.000	0.119	0.124	0.026	0.074
Total *W*	1.000	1.000	1.000	1.000	1.000	1.000	1.000	1.000
f	0.50	0.56	0.40	0.50	0.37	0.45	0.52	0.45
Ca/(Ca + Na)	0.13	0.12	0.04	0.12	0.01	0.12	0.30	0.21

Note: The formula units were calculated on the basis of the general tourmaline formula $[XY_3Z_6B_3T_6O_{27}(V, W)_4]$, where *X* is Na^+, K^+, Ca^{2+}, and occasional vacancies; *Y* is Mg^{2+}, Fe^{2+}, Fe^{3+}, Al^{3+}, Mn, Cr, V, Li^+, and Ti^{4+}; *Z* is Al and admixtures of Fe^{3+}, Fe^{2+}, Ti, Mg, Cr, and V; *T* is Si and a small admixture of Al; *V* is OH^- and a small admixture of O; and *W* is O and admixtures of OH^- and F^-. $f = Fe_{tot}/(Fe_{tot} + Mg)$; c, the core of a crystal; m, the margin.

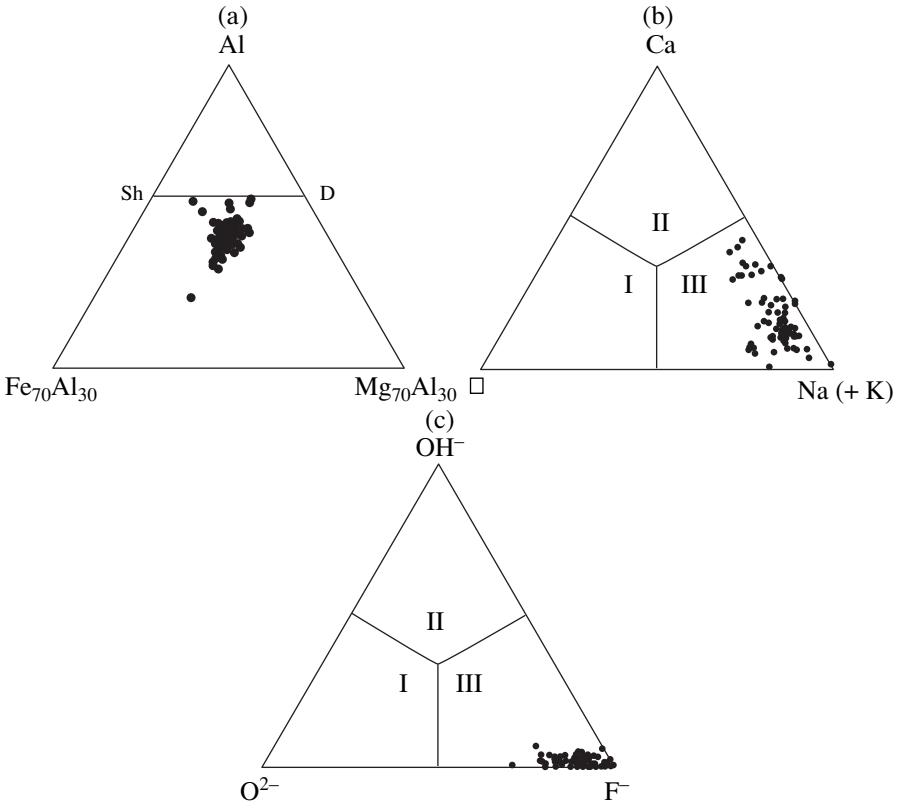

Fig. 9. Composition of tourmalines from the Talatui deposit. (a) Fe–Al–Mg (Sh, schorl; D, dravite); (b) □(vacancy)–Ca–Na(+K) ((I) vacant; (II) calcic; (III) alkaline); (c) OH–F–O ((I) O^{2-}; (II) OH^-; (III) F^-).

maline is locally replaced with sulfides. Two types of chemical zoning are distinguished in tourmaline crystals. Crystals of the first type are associated with magnetite and phlogopite and characterized by an insignificant outward increase in $Fe_{tot}/(Fe_{tot} + Mg)$ ratio (0.45 ⟶ 0.56, 0.56 ⟶ 0.64). Grains of the second type are associated with the early pyrite and chalcopyrite and are distinguished by reverse zoning (0.53 ⟶ 0.50 ⟶ 0.48 ⟶ 0.44; 0.45 ⟶ 0.55 ⟶ 0.39) against the background of an oscillating $Fe_{tot}/(Fe_{tot} + Mg)$ ratio. In general, this ratio varies in tourmaline from 0.36 to 0.64. The values of ^{W}OH (fu) and the Ca/(Ca + Na) ratio vary from 0 to 0.985 and 0.01 to 0.45, respectively (Table 2). The chemical data are summarized in the diagrams shown in Fig. 9. The Moessbauer spectroscopy of an averaged tourmaline sample yielded an Fe^{3+}/Fe_{tot} ratio equal to 0.67. In addition, the Moessbauer spectra did not reveal Fe^{3+} in position *Z* of the tourmaline structure. Thus, according to the classification proposed by Hawthorne and Henry (1999), the studied tourmaline may be referred to as an intermediate member of the dravite (oxidravite)–schorl (oxischorl)–uvite–feruvite series. Zn (up to 0.010 fu), Cu (up to 0.037 fu), and F (up to 0.230 fu) are noted as admixtures.

Phlogopite contains (wt %) 9.2–9.9 K_2O, 18.0–18.8 MgO, 0.23–0.92 F, and 3.1–3.8 H_2O and corresponds in its composition to phlogopite from porphyry copper deposits (Popov, 1977; Krivtsov et al., 1986, 2001).

Scheelite occurs in ore as small (up to 2 mm) white euhedral crystals often crossed by sulfide veinlets along fractures (Fig. 10). The chemical composition of scheelite (Table 3) is (wt %) 0.17–0.44 MoO_3, 0.03–0.45 FeO, up to 0.11 BaO, and up to 0.05 PbO; SrO was not detected. The blue luminescence in ultraviolet light is consistent with low powellite content.

Molybdenite is observed in association with chalcopyrite and epidote (Fig. 6d) as euhedral flakes up to a few millimeters in length that contain (wt %) 0.29–1.23 Cu, up to 0.50 Se, up to 0.04 Sn, up to 0.70 W, and up to 0.60 Re (Table 4). All analyses that detected Re pertain to outer zones of crystals, whereas no Re (<0.01 wt %) was detected with the microprobe in their central portions. High Re contents are typical of molybdenite from porphyry copper deposits (Popov, 1977; Krivtsov et al., 1986, 2001).

Magnetite occurs as numerous small crystals or small inclusions in pyrite (Fig. 8a). Magnetite contains (wt %) up to 0.09 MgO, 0.04–0.94 Al_2O_3, 0.01–0.29 SiO_2, up to 0.13 TiO_2, up to 0.23 CaO, up to 0.07 V_2O_3, up to 0.14 Cr_2O_3, 0.02–0.15 MnO, up to 0.07 NiO, up to 0.12 ZnO, up to 0.55 Ga_2O_3, and up to 0.16 Nb_2O_5.

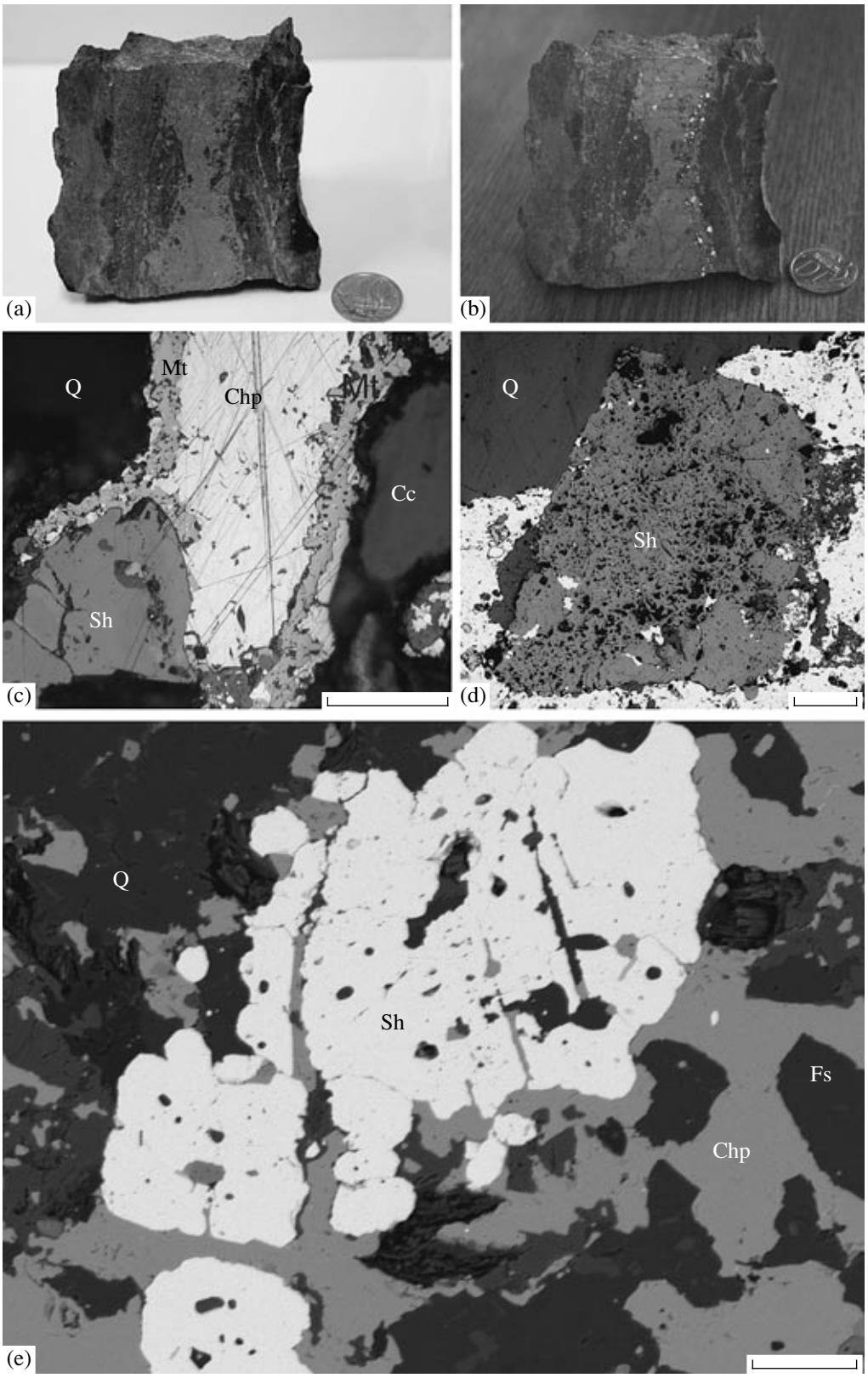

Fig. 10. Scheelite in ore from the Talatui deposit. (a, b) Hand specimen of chalcopyrite ore with scheelite: (a) in daylight, (b) under ultraviolet irradiation; (c) intergrowth of scheelite with magnetite and chalcopyrite; (d) scheelite crystal overgrown by pyrite and quartz; (e) scheelite in a chalcopyrite–feldspar aggregate (BSE image). (Sh) Scheelite, (Mt) magnetite, (Fs) feldspar, (Chp) chalcopyrite, (Q) quartz, (Cc) calcite. Scale bar, 100 μm.

Table 3. Chemical composition of scheelite from the Talatui deposit, wt %

Analysis	CaO	WO_3	FeO	MoO_3	BaO	Total
1	19.55	79.45	0.45	0.32	0.05	99.82
2	19.40	80.36	0.17	0.27	0.07	100.25
3	19.38	80.09	0.03	0.24	n.d.	99.73
4	19.49	79.56	0.20	0.23	″	99.47
5	19.24	79.10	0.41	0.44	0.06	99.24
6	19.34	80.35	0.03	0.35	0.11	100.18
7	19.55	78.39	0.04	0.18	0.05	98.21
8	19.66	79.44	0.05	0.29	0.05	99.49
9	19.63	79.44	0.08	0.17	n.d.	99.32

Note: n.d., not detected.

Table 4. Chemical composition of molybdenite from the Talatui deposit, wt %

Analysis	Mo	S	Cu	Se	Sn	W	Re	Total
1	59.08	38.80	1.23	n.d.	n.d.	n.d.	n.d.	99.11
2	59.36	38.92	0.69	0.12	0.04	0.39	0.40	99.92
3	59.24	38.03	0.43	0.34	0.04	0.70	0.60	99.38
4	59.16	39.54	0.73	n.d.	n.d.	0.05	n.d.	99.48
5	58.51	39.85	0.70	″	0.04	n.d.	0.36	99.47
6	58.14	39.81	0.37	0.50	n.d.	″	0.25	99.04
7	58.31	40.08	0.29	n.d.	0.04	″	n.d.	98.72

Note: n.d., not detected.

Pyrite is present as euhedral crystals or crystalline aggregates. The mineral often contains inclusions of rutile, tourmaline, magnetite, gold, barite, anhydrite, and bismuth minerals. The following chemical elements have been detected in pyrite (wt %): up to 1.52 Co, up to 0.25 Ni, up to 0.60 As, up to 0.07 Sb, up to 1.73 Au, up to 0.29 Bi, up to 0.07 Se, and up to 0.30 Cu. The high Au contents in pyrite are most likely caused by submicroscopic (<1 μm) inclusions of native gold. In addition, microinclusions of Bi minerals (wittichenite, pilsenite) and sulfates (barite, anhydrite) are identified in pyrite.

Native gold is identified in ore relatively often. Two generations of gold have been revealed (Table 5, Fig. 11). The older gold is associated with rutile, epidote, magnetite, scheelite, and potassium feldspar and has the highest fineness (964–996). Gold grains as large as 50 μm occur as disseminations in the minerals listed above. The fineness of the younger gold, associated with magnetite, pyrite, and chalcopyrite, is lower (777–874). This gold is present as small (up to 10 μm) inclusions in magnetite, pyrite, and chalcopyrite and large (up to 0.3 mm) grains, which occasionally are cut by small electrum veinlets (the fineness is 440), most likely formed contemporaneously with other Ag minerals. It should be noted that the established range of gold fineness (Fig. 12) covers all the data previously published in the literature. Impurities in native gold include (wt %) 0.03–0.88 Cu, 0.03–1.66 Fe, 0.01–0.15 Te, 0.01–0.17 Sb, 0.06–0.78 Hg, and 0.01–0.32 Bi.

Sphalerite has been detected as a single grain within the younger chalcopyrite. This grain contains (wt %) 1.83 Fe, 0.65 Cu, and 0.41 Cd.

Siegenite ($CoNi_2S_4$) was identified in samples with >0.5 wt % Co. This is a mineral of the linnaeite group, isotropic and cream-white with a pinkish hue. Isometric grains of siegenite up to 50 μm in size occur within chalcopyrite or at chalcopyrite–pyrite boundaries (Fig. 6f). It was deemed previously (Borishanskaya et al., 1981) that minerals close to $NiCo_2S_4$ may be termed Ni-bearing linnaeite. According to Wagner and Cook (1999), thiospinels with formula units of Ni >1 and Cu <0.5 should be referred to as Cu-bearing siegenite. The mineral closest in composition to siegenite from the Talatui deposit was found in pyrite–chalcopyrite ore at the Udokan deposit in association with pyrite, chalcopyrite, linnaeite, and sphalerite (Boldyreva et al., 1986).

Silver minerals—hessite (Ag_2Te) and matildite ($AgBiS_2$)—previously unknown at the Talatui deposit were identified in the course of our investigations (Fig. 14). The grains of these minerals only occasion-

Table 5. Chemical composition of native gold from the Talatui deposit, wt %

No.	Assemblage	Au	Ag	Cu	Fe	Bi	Te	Hg	Sb	S	Total	Sample
						Gold I						
1	Ep, Ru	99.22	0.09	0.12	0.03	0.01	0.05	n.d.	0.03	0.03	99.58	996
2	Ep, Ru	99.37	0.23	0.17	0.09	0.16	n.d.	0.16	0.05	0.06	100.29	991
3	Ep, Mt	98.57	0.88	0.09	0.37	0.13	0.02	0.07	0.11	0.03	100.26	983
4	Ep	97.27	2.23	0.13	0.11	0.09	0.09	n.d.	n.d.	0.11	100.03	972
5	Ep, Mt	97.71	2.37	0.13	0.13	0.10	0.04	″	″	0.05	100.53	972
6	Ep, Mt	97.83	1.92	0.15	0.27	0.35	0.13	″	0.02	0.03	100.71	971
7	Ep, Mt	97.40	2.62	0.20	0.19	n.d.	0.07	″	0.04	0.04	100.56	969
8	Ep, Mt	96.36	2.39	0.16	0.41	0.02	0.05	″	n.d.	0.01	99.40	969
9	Ep, Mt	96.00	2.29	0.02	0.77	n.d.	n.d.	″	″	0.09	99.18	968
10	Ep, Mt	97.16	2.48	0.13	0.22	0.04	0.06	0.19	0.07	n.d.	100.35	968
11	Ep, Mt	96.90	2.25	0.07	0.94	n.d.	0.07	0.24	n.d.	0.08	100.53	964
12	Ep	96.42	3.20	0.13	0.29	0.06	0.03	n.d.	n.d.	0.06	100.19	962
13	Ep, Mt	96.15	2.35	0.18	1.09	0.07	n.d.	″	0.05	0.02	99.92	962
14	Ep, Mt	95.44	2.53	0.09	0.93	n.d.	″	0.12	n.d.	0.07	99.19	962
15	Ep, Mt	95.68	2.43	0.17	0.42	0.18	″	0.54	0.05	0.05	99.52	961
16	Ep, Mt	96.18	2.64	0.11	1.08	n.d.	″	n.d.	0.06	0.01	100.07	961
17	Ep, Mt	96.13	2.64	0.18	0.89	0.10	0.09	0.09	n.d.	0.05	100.17	960
18	Ep, Mt	95.76	2.95	0.09	0.52	n.d.	0.10	0.13	0.17	0.06	99.79	960
19	Ep, Mt	95.10	3.24	0.12	0.30	0.15	0.02	0.06	0.05	0.07	99.11	960
20	Ep	95.16	3.07	0.12	0.59	0.20	0.04	n.d.	0.04	0.10	99.32	958
21	Ep, Mt	96.20	2.61	0.05	0.80	0.07	0.08	0.44	0.09	0.06	100.40	958
22	Ep, Mt	96.29	2.31	0.19	1.65	0.11	n.d.	n.d.	0.08	n.d.	100.63	957
23	Ep, Mt	93.75	2.46	0.03	1.32	n.d.	″	0.36	0.06	0.02	98.00	957
24	Ep, Mt	95.67	2.73	0.09	0.98	0.32	0.04	0.24	0.06	0.04	100.17	955
25	Ep, Mt	94.95	2.58	0.06	1.53	n.d.	0.04	0.46	0.05	0.12	99.79	951
						Gold II						
26	Chp, Mt	87.68	11.68	0.04	0.14	0.30	0.09	0.08	0.02	0.09	99.11	885
27	Py	86.80	12.01	0.13	0.10	n.d.	0.08	0.14	n.d.	0.10	99.36	874
28	Mt, Py	86.90	12.26	0.05	0.05	0.01	0.05	n.d.	0.08	0.06	99.46	874
29	Chp, Mt	86.73	12.12	0.06	0.17	0.02	0.04	0.11	n.d.	0.13	99.39	873
30	Chp, Mt	86.63	12.41	0.06	0.07	0.04	0.08	n.d.	″	0.06	99.34	872
31	Chp, Mt	85.99	12.35	0.07	0.14	0.13	n.d.	0.13	″	0.07	98.87	870
32	Chp, Mt	87.08	12.33	0.06	0.29	0.07	0.09	0.15	0.05	0.22	100.34	868
33	Chp, Mt	86.09	12.69	0.03	0.05	0.22	0.05	0.10	n.d.	0.08	99.30	867
34	Mt, Py	86.52	12.80	0.04	0.04	n.d.	0.09	0.46	0.04	0.06	100.05	865
35	Py	85.76	12.62	0.22	0.24	0.22	0.05	n.d.	0.01	0.20	99.20	865
36	Py, Chp	86.21	12.78	0.27	0.25	n.d.	0.12	″	n.d.	0.13	99.75	864
37	Chp, Mt	86.33	12.74	0.05	0.10	0.13	0.09	0.46	″	0.05	99.95	864
38	Chp, Mt	86.65	12.49	0.28	0.16	0.30	0.10	0.35	0.06	0.15	100.53	862
39	Chp, Mt	85.76	12.88	0.10	0.08	0.17	0.15	0.32	n.d.	0.04	99.50	862
40	Mt, Py	86.00	12.78	0.07	0.08	0.15	0.13	0.78	0.08	0.08	100.14	859
41	Py, Chp	85.49	13.70	0.16	0.07	0.10	0.06	n.d.	0.02	0.08	99.69	858
42	Mt, Q	85.76	13.91	0.10	0.10	0.10	0.04	″	0.06	0.03	100.09	857

Table 5. (Contd.)

No.	Assemblage	Au	Ag	Cu	Fe	Bi	Te	Hg	Sb	S	Total	Sample
43	Mt	85.45	13.60	0.08	0.22	0.15	0.09	0.26	0.04	0.08	99.97	855
44	Chp, Mt	85.60	13.97	0.10	0.26	0.11	0.08	n.d.	n.d.	0.10	100.23	854
45	Mt	85.46	14.03	0.06	0.51	0.02	0.10	″	″	0.09	100.28	852
46	Chp, Mt	85.07	12.88	0.08	0.89	0.19	0.01	0.68	0.04	0.13	99.97	851
47	Chp	84.76	14.68	0.10	0.03	n.d.	0.08	n.d.	0.06	0.07	99.79	849
48	Chp, Py	84.67	13.25	0.36	0.84	0.13	0.07	0.37	0.01	0.17	99.86	848
49	Chp	84.93	14.76	0.11	0.14	0.16	0.09	0.17	0.01	0.06	100.43	846
50	Chp	84.20	14.97	0.12	0.03	n.d.	0.12	n.d.	n.d.	0.08	99.62	845
51	Mt	83.63	15.00	0.15	0.77	0.12	0.07	0.34	0.01	0.09	100.18	835
52	Mt, Py	83.55	14.95	0.61	0.65	0.11	0.05	n.d.	0.07	0.06	100.04	835
53	Py, Mt	82.63	16.35	0.02	0.49	n.d.	0.09	0.10	n.d.	0.12	99.79	828
54	Mt, Q	82.87	16.41	0.02	0.63	0.08	0.05	0.41	0.06	0.05	100.59	824
55	Chp	81.14	17.97	0.07	0.31	n.d.	0.01	n.d.	n.d.	0.10	99.61	815
56	Chp, Mt	81.01	18.33	0.02	0.09	0.05	0.05	0.35	0.02	0.06	99.99	810
57	Mt, Q	79.73	17.56	0.05	1.46	n.d.	0.11	n.d.	0.01	1.27	100.19	796
58	Chp, Mt	78.25	20.17	0.88	0.68	0.12	0.03	n.d.	n.d.	0.10	100.24	781
59	Chp, Mt	78.00	20.79	0.50	0.86	0.16	0.04	″	″	0.09	100.44	777

Note: Minerals: (Ru) rutile, (Ep) epidote, (Mt) magnetite, (Py) pyrite, (Chp) chalcopyrite, (Q) quartz. n.d., not detected.

ally reach 20 μm in size; commonly, they are much smaller. They often make up veinlets in pyrite and chalcopyrite and were precipitated at the end of the ore-forming process. The above-mentioned electrum veinlet crosscutting a grain of native gold probably was formed at the same time. The divergence in time of crystallization of Au and Ag minerals (native gold precipitated at the early stage of the ore-forming process, whereas the silver minerals did so at the end of this process) caused a difference in the spatial distribution of these elements in ore, especially evident in ore zone 2.

STUDY OF FLUID INCLUSIONS

The examination of a great number of transparent polished plates under an Olympus BX51 optical microscope equipped with high-resolution objectives allowed study of fluid inclusions 8–15 μm in size captured by quartz of different mineral assemblages.

Three types of fluid inclusions are recognized (Fig. 15): (1) inclusions of chloride brine that contain a gas bubble, water solution, one or several isotropic crystals, and occasionally an opaque ore mineral; (2) substantially gas inclusions that contain gas with a thin rim of aqueous solution and an occasional cubic isotropic crystal; and (3) two-phase gas–liquid inclusions of diluted solutions. Fluid inclusions uniformly distributed throughout the volume of quartz grains and classified by us as primary inclusions were chosen for thermo- and cryometric studies.

The results of these studies, which involved 374 individual fluid inclusions in quartz and calcite (Table 7, Fig. 16), indicate that Mg, Na, and occasionally Ca chlorides participated in the ore formation. This is attested to by chloride eutectic temperatures of solutions ranging from –43 to –21°C and from –62 to –47°C, as well as by the occurrence of daughter halite crystals of cubic habit, identified by their similarity in refractive index to quartz and by their transition to hydrohalite during freezing of solutions (the reverse transition to halite occurs at 0–0.5°C). The complete homogenization of brine inclusions (complete dissolution of daughter phases) is achieved at a temperature of 611–269°C, and the salt concentration amounts to 56.3–29.9 wt % NaCl equiv. The pressure was estimated at 3370–300 bar based on inclusions of saturated solutions; the fluid density varies from 1.25 to 0.78 g/cm^3.

The substantially gaseous fluid inclusions are homogenized into gas at 589–292°C and contain a fluid with salt concentrations ranging from 33.8 to 0.9 wt % NaCl equiv. Some inclusions contain carbon dioxide of a low density (0.42–0.02 g/cm^3), which is homogenized into gas over the temperature interval from 30.1 to –49.3°C. The melting of the frozen carbon dioxide occurs at temperatures from –58.9 to –56.6°C, indicating that a small admixture of other gases (<5 mol %) is present. The pressure estimates based on the inclusions of this type are 1170–110 bar; the fluid density varied from 0.55 to 0.16 g/cm^3.

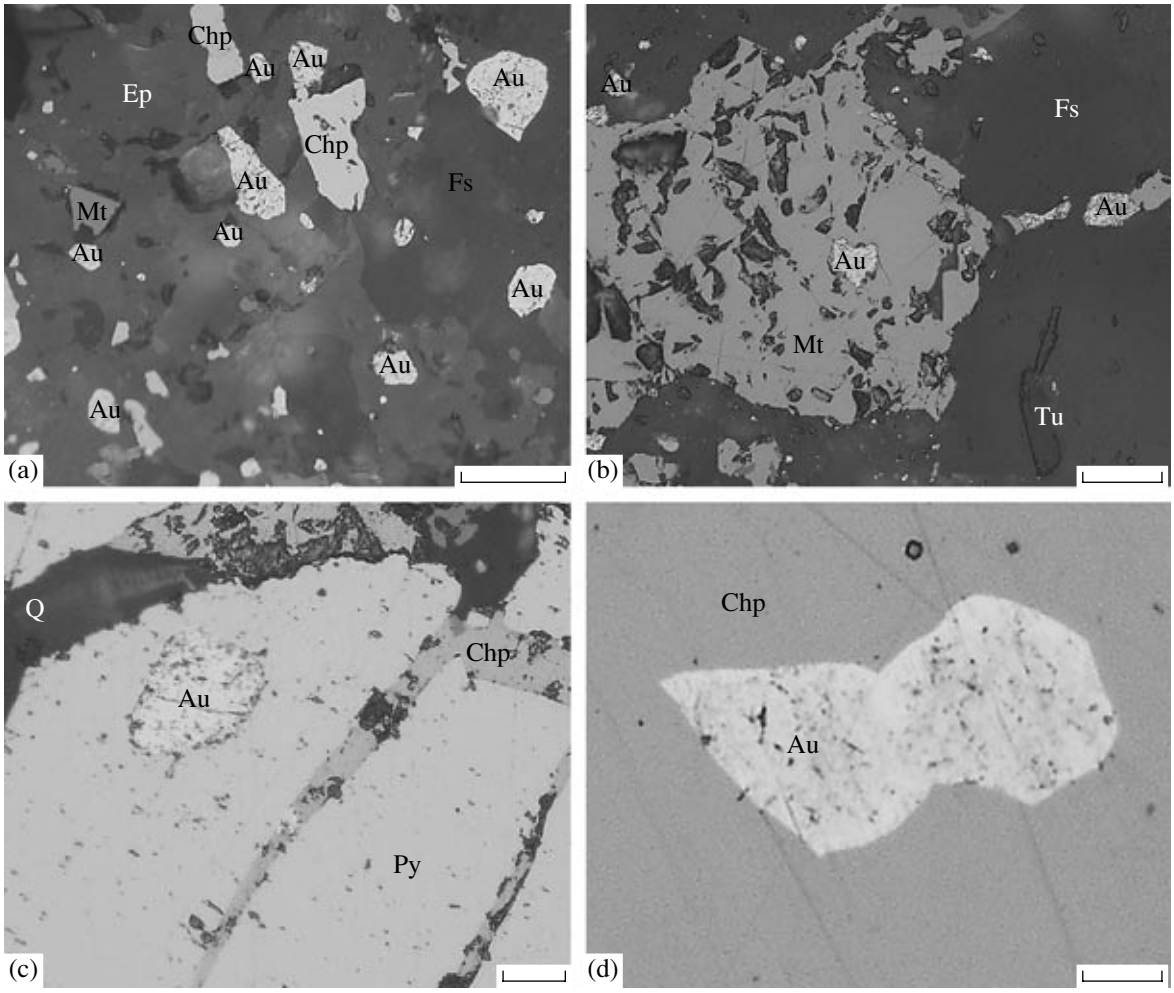

Fig. 11. Gold in different mineral assemblages in ore from the Talatui deposit. (a) Gold in epidote and feldspar; (b) gold in magnetite and felspar; (c) gold in pyrite; (d) gold in chalcopyrite. Scale bar, 20 μm. (Au) gold, (Ep) epidote, (Mt) magnetite, (Fs) feldspar, (Py) pyrite, (Tu) tourmaline, (Chp) chalcopyrite, (Q) quartz.

The two-phase gas–liquid inclusions of diluted solutions are homogenized into liquid at 495–145°C, while the eutectic temperature varies within the temperature range from –48 to –21°C, showing the chloride composition of solutions and the presence of Ca, Na, and Mg ions therein. The salt concentration in solutions that fill inclusions varies from 23.2 to 0.4 wt % NaCl equiv, and the fluid density, from 1.03 to 0.49 g/cm^3.

Table 6. Chemical composition of siegenite from the Talatui deposit, wt %

Analysis	S	Fe	Co	Ni	Cu	Mn	Zn	Se	Total
1	41.37	2.71	29.55	21.32	5.60	n.d.	n.d.	n.d.	100.54
2	41.91	2.76	29.27	21.77	5.21	0.02	″	0.02	100.96
3	41.72	2.86	29.91	19.80	6.77	0.03	″	n.d.	101.09
4	41.61	1.73	29.36	21.15	6.60	n.d.	0.05	0.04	100.55
5	41.52	2.15	29.74	19.60	7.54	″	0.13	0.07	100.75
6	41.71	1.65	29.55	21.50	6.58	″	n.d.	n.d.	100.99
7	41.96	1.74	29.50	21.62	6.34	0.01	″	″	101.17

Note: 1 – $Co_{1.53}Ni_{1.11}Cu_{0.27}Fe_{0.15}S_{3.94}$; 2 – $Co_{1.51}Ni_{1.13}Cu_{0.25}Fe_{0.15}S_{3.97}$; 3 – $Co_{1.55}Ni_{1.03}Cu_{0.32}Fe_{0.16}S_{3.95}$; 4 – $Co_{1.49}N_{1.08}Cu_{0.31}Fe_{0.09}S_{3.89}$; 5 – $Co_{1.54}Ni_{1.02}Cu_{0.36}Fe_{0.12}S_{3.96}$; 6 – $Co_{1.53}Ni_{1.11}Cu_{0.32}Fe_{0.09}S_{3.96}$; 7 – $Co_{1.53}Ni_{1.12}Cu_{0.30}Fe_{0.09}S_{3.97}$. n.d., not detected.

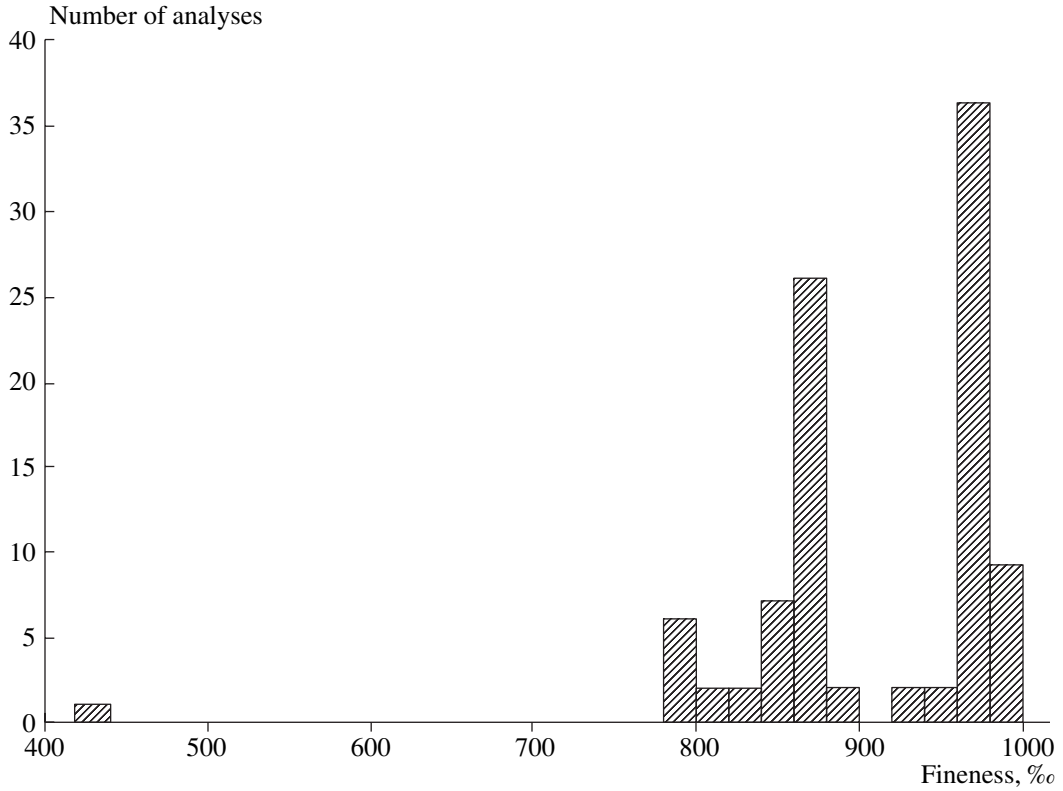

Fig. 12. Histogram of gold fineness at the Talatui deposit.

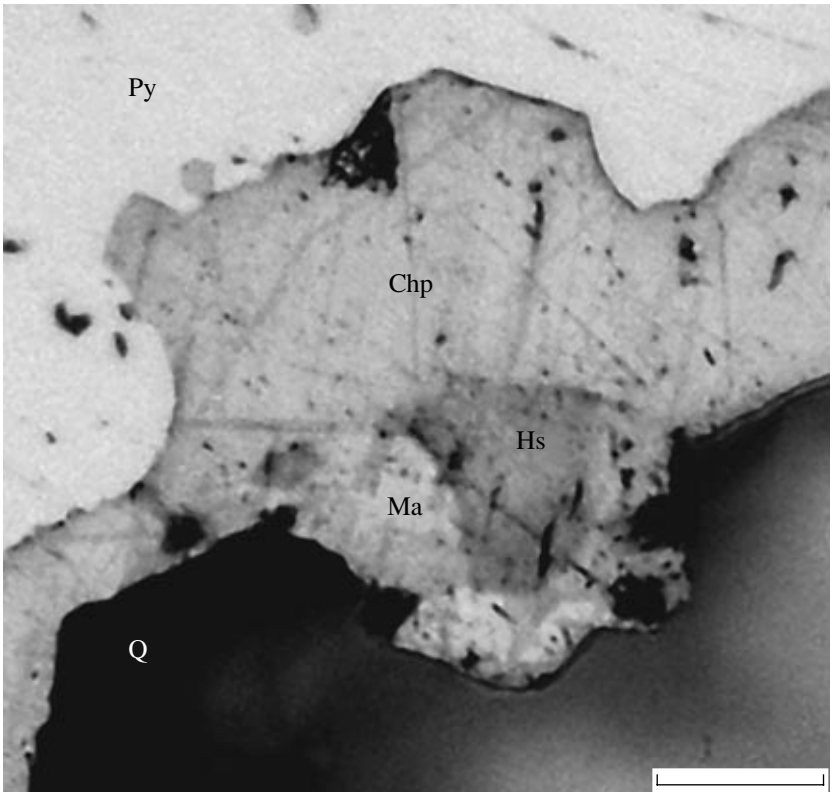

Fig. 13. Matildite ($AgBiS_2$) and hessite (Ag_2Te) in association with chalcopyrite and quartz. (Ma) Matildite, (Hs) hessite, (Py) pyrite, (Q) quartz. Scale bar, 20 μm.

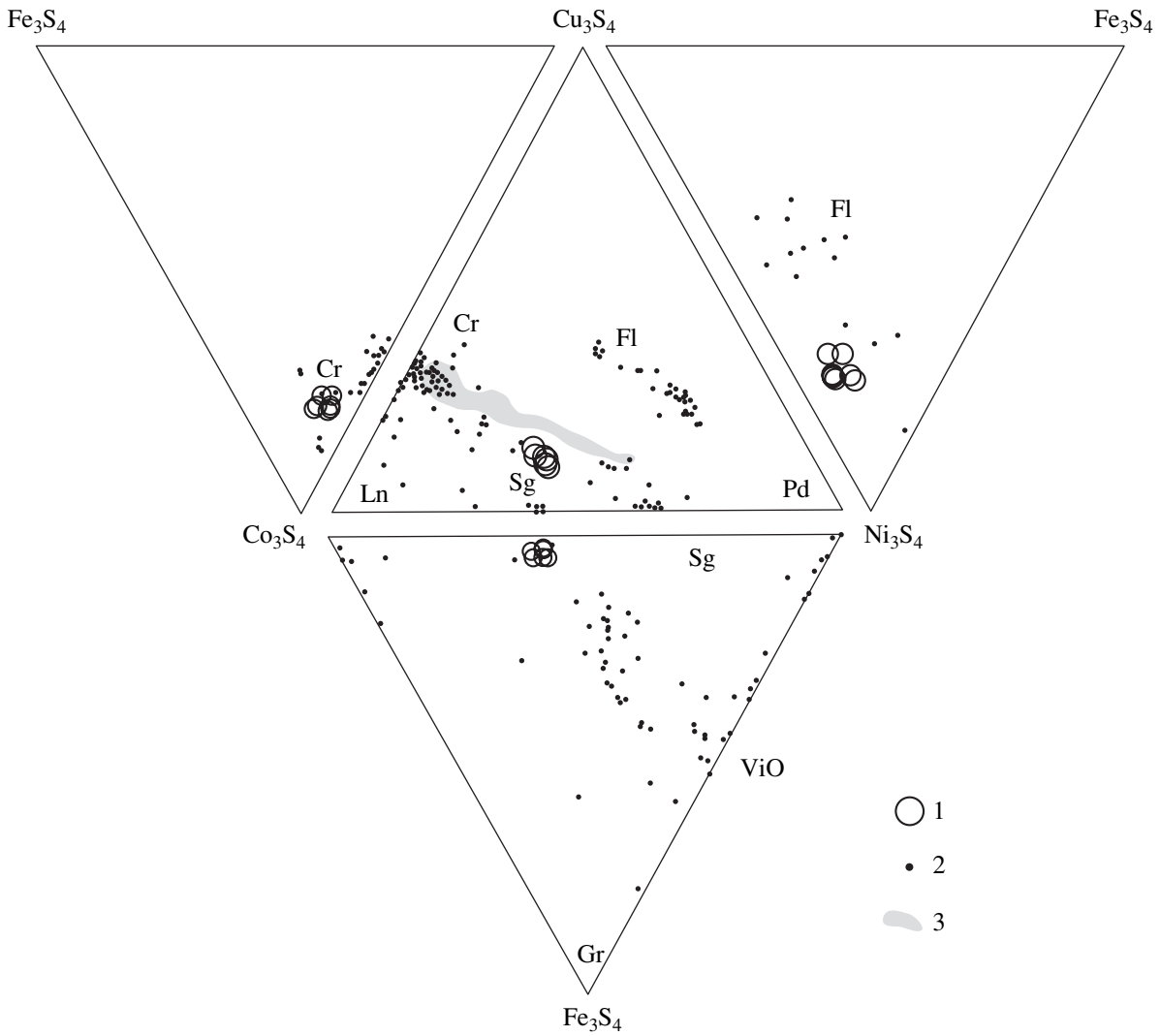

Fig. 14. Composition of siegenite from the Talatui deposit in comparison with minerals of the linnaeite group. (1) Siegenite from the Talatui deposit; (2) analyses from elsewhere; (3) siegenite from a deposit in Siegerland, Germany; (2, 3) after Wagner and Cook (1999). (Sg) Siegenite, (Cr) carrollite, (Gr) greigite, (Fl) fletcherite, (Ln) linnaeite, (Pd) polydymite, (Vio) violarite.

The aqueous extracts from inclusions of chloride brines captured by quartz of the productive quartz–tourmaline–pyrite assemblage bear important information on the composition of ore-forming fluid (Table 8). Judging from a preliminary visual examination, two other types of fluid inclusions in quartz occur in subordinate amounts. The studied fluid contains (g/kg H_2O) 54.5–36.7 Na, 27.7–20.5 K, and 18.1–11.1 Ca; Mg is contained in much smaller amounts (2.7–0.9 g/kg H_2O). Appreciable concentrations (g/kg H_2O) of the following components have been established: 108.3–71.8 Cl^-, 49.8–10.5 CO_2, and 0.35–0.08 CH_4, as well as 0.48–0.04 Br, 0.38–0.15 As, 1.39–0.25 Sr, 2.28–0.93 Zn, 4.44–1.86 Mn, 1.1–0.8 Fe, 1.3–0.14 Ba, and 1.48–0.11 B. In addition, many microcomponents have been detected in the fluid (mg/kg of solution): 63–24 Li, 120–67 Rb, 29–14 Cs, 71–12 Sc, 3.6–1.1 Co, 17–10 Ni, 7.2–6.8 Cr, 181–166 Cu, 2.6–0.3 Ag, 0.3–0.04 Y, 1.4–0.18 Zr, 2.6–0.7 Mo, 7.8–5.2 Cd, 6.9–4.9 Sb, 1.5–1.1 Ga, 2.6–1.0 Ge, 26.6–7.6 Ti, 0.21–0.01 Nb, 2.7 Sn, 0.4 Au, 0.47–0.32 Hg, 0.01 Hf, 1.9–0.3 REE, 6.9–0.07 W, 3.3–1.7 Tl, 62–2.3 Pb, 0.28–0.07 Bi, 0.25–0.16 Th, and 1.03–0.04 U.

The results of the study of fluid inclusions (Fig. 16a) indicate that chloride brine with a rather high salt concentration and a gas phase were prevalent in the temperature interval from 600 to 300°C. An aqueous solution appeared below 500°C and began to play an increasingly important role in ore formation with falling temperature. At ~300°C, the salt concentration in fluid dropped drastically, probably, owing to dilution with low-mineralized solutions, presumably of meteoric nature.

THERMODYNAMIC MODELING

The *PTX* parameters of the model chemical system were chosen on the basis of the results of the fluid inclu-

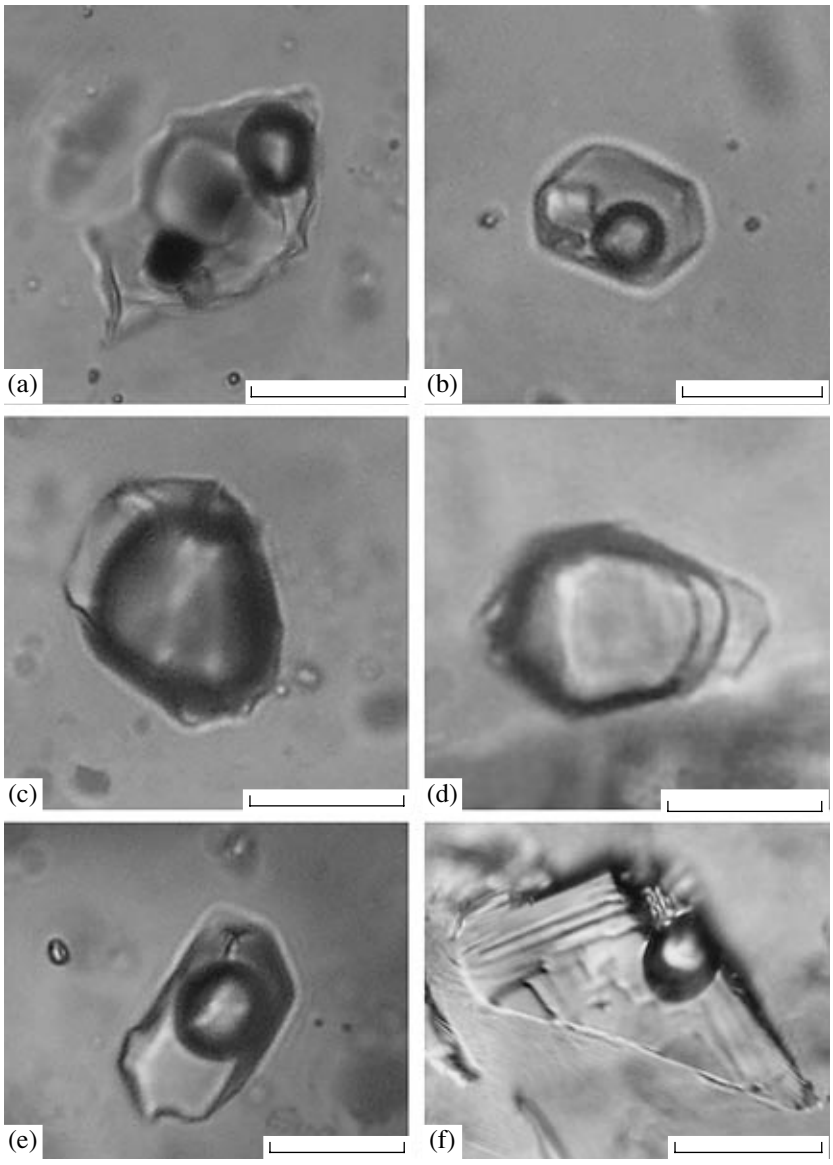

Fig. 15. Fluid inclusions in (a–e) quartz and (f) calcite of ore from the Talatui deposit. (a) Multiphase inclusion of chloride brine with daughter ore minerals (T_{hom} = 594°C, C_{salt} = 38.7 wt %); (b) three-phase inclusion of chloride brine (T_{hom} = 341°C, C_{salt} = 30.3 wt %); (c) substantially gas inclusion (T_{hom} = 493°C, C_{salt} = 25.0 wt %); (d) substantially gas inclusion with liquid CO_2 (T_{hom} = 431°C, C_{salt} = 21.8 wt %); (e) two-phase gas–liquid inclusion (T_{hom} = 360°C, C_{salt} = 9.2 wt %); (f) two-phase gas–liquid inclusion (T_{hom} = 177°C, C_{salt} = 0.9 wt %). Scale bar, 10 μm.

sion study. Thermodynamic modeling of the transport and concentration of Au, Ag, and Cu in the given hydrothermal system was performed. The thermodynamic model is based on the equilibria in the 16-component system Na–K–Ca–Mg–Al–Fe–Cu–Ag–Au–B–Si–C–S–Cl–O–H. The phase composition of the system corresponded to equilibrium with a rock similar to the average gabbro, after Zavaritsky (Voitkevich et al., 1990). The sulfur and oxygen fugacities were set by the pyrite–pyrrhotite–magnetite (Py–Po–Mt) buffer. The computation was carried out using a modified version of the BALANCE program (Akinfiev, 1986), intended for the study of equilibria in multisystems. The SUPCRT92 package (Johnson et al., 1992), for calculation of the thermodynamic properties of components, and the expanded DPRONS98 thermodynamic database (Shock et al., 1997; Sverjensky et al., 1997; Bastrakov et al., 2004) were linked up to the program. A summary prepared by Akinfiev and Zotov (2001) was used for description of the behavior of Au-, Ag-, and Cu-bearing species of hydrothermal fluid, and results reported in (Akinfiev et al., 2006) were applied to B-bearing species. The thermodynamic properties of schorl $[NaFe_3Al_6(BO_3)_3Si_6O_{18}(OH)_4]$ and dravite

Table 7. Results of thermo- and cryometric studies of individual fluid inclusions in quartz and calcite from ore veins at the Talatui deposit, the eastern Transbaikal region

Sample	Mineral	Type*	*n*	T_{hom}, °C	T_{eut}, °C	$T_{ice\ melt}$ (NaCl), °C	$T_{melt\ CO_2}$, °C	$T_{hom\ CO_2}$, °C	$T_{gas\ hydrate\ melt}$, °C	C_{salt}, wt % NaCl equiv ($CaCl_2$)	d, g/cm^3	P, bar	$(P_{H_2O} + P_{gas})/P_{H_2O}$
30/01	Quartz	1	2	594	–54	(309)	–	–	–	38.7	0.80	–	–
	″	1	2	513	–35	(257)		–	–	35.2	0.84	–	–
	″	1	3	477	–48	(339)		–	–	41.4	0.94	–	–
	″	1	2	329	n.a.	(412)	–	–	–	48.7	1.18	1969	1.0
	″	1	2	402	–55	(282)	–	–	–	36.8	0.97	–	–
	″	1	13	381	–36	(247)	–	–	–	34.6	0.97	–	–
	″	1	7	361	–53	(355)	–	–	–	42.9	1.08	–	–
	″	1	4	265	n.a.	(352)	–	–	–	42.6	1.17	1824	1.0
	″	1	18	261	–56	(341)	–	–	–	41.6	1.16	1658	1.0
	″	1	2	341	–55	(164)	–	–	–	30.3	0.97	–	
	″	1	3	304	n.a.	(252)	–	–	–	34.8	1.05	–	–
	″	2	2	589 G	–54	(133)	–	–	–	29.0	0.19	1171	1.0
	″	2	3	543 G	–54	(236)	–	–	–	33.8	0.24	871	1.0
	″	2	4	493 G	–39	–28.9	–	–	–	25.0	0.20	608	1.0
	″	2	4	458 G	–35	–3.6	–57.2	–49.1 G	–	5.9	0.20	486	1.06
	″	2	2	456 G	–50	–29.7	–58.9	30.1 G	–14.8	(25.2)	0.57	998	2.20
	″	2	3	456 G	–36	–3.7	–	–	–	6.0	0.16	453	1.0
	″	2	5	431 G	–51	–21.1	–	–	–	(21.8)	0.20	364	1.0
	″	2	3	348 G	–38	–9.7	–	–	–	13.6	0.22	154	1.0
	″	2	9	342 G	–32	–4.7	–	–	–	7.5	0.22	–	–
	″	2	3	321 G	–35	–13.8	–57.6	24.7 G	–	17.6	0.20	373	3.4
	″	3	2	495	–42	–11.4	–	–	–	15.4	0.54	–	–
	″	3	4	469	–35	–3.7	–	–	–	6.0	0.49	–	–
	″	3	4	383	–26	–5.9	–	–	–	9.1	0.66	–	–
	″	3	6	370	–35	–6.0	–	–	–	9.2	0.69	–	–
	″	3	4	362	–35	–6.0	–	–	–	9.2	0.71	–	–
	″	3	3	361	–31	–0.5	–	–	–	0.9	0.55	–	–
	″	3	5	360	–35	–6.0	–	–	–	9.2	0.72	–	–
	″	3	3	315	–33	–0.4	–	–	–	0.7	0.66	–	–
	″	3	3	324	–29	–1.3	–	–	–	2.2	0.67	–	–
	″	3	3	302	–48	–16.4	–	–	–	19.8	0.91	–	–
	″	3	2	133	–21	–0.2	–	–	–	0.4	0.94	–	–
	″	3	2	32	–21	–3.2	–	–	–	5.3	1.03	–	–

Table 7. (Contd.)

Sample	Mineral	Type*	n	T_{hom}, °C	T_{eut}, °C	$T_{ice\ melt}$ (NaCl), °C	$T_{melt\ CO_2}$, °C	$T_{hom\ CO_2}$, °C	$T_{gas\ hydrate\ melt}$, °C	C_{salt}, wt % NaCl equiv ($CaCl_2$)	d, g/cm^3	P, bar	$(P_{H_2O} + P_{gas})/P_{H_2O}$
3TL/85	Quartz	1	3	590	–54	(284)	–	–	–	37.0	0.78	–	–
	″	1	5	542	–55	(394)	–	–	–	46.8	0.94	865	–
	″	3	2	343	–36	–1.0	–	–	–	1.7	0.61	–	–
	″	3	3	251	–30	–0.3	–	–	–	0.5	0.79	–	–
	″	3	6	244	–29	–0.4	–	–	–	0.7	0.81	–	–
	″	3	5	196	–30	–0.8	–	–	–	1.4	0.88	–	–
28/01	Quartz	1	2	358	–56	(474)	–	–	–	56.3	1.25	3366	1.0
	″	1	5	301	–56	(437)	–	–	–	51.6	1.24	3341	1.0
	″	1	3	271	–55	(392)	–	–	–	46.6	1.21	2659	1.0
	″	1	3	312	–57	(376)	–	–	–	44.9	1.15	1412	1.0
	″	1	8	321	–54	(195)	–	–	–	31.7	1.01	–	–
	″	2	3	489 G	–43	–20.2	–	–	–	22.5	n.a.	590	1.0
	″	2	2	455 G	–55	(182)	–58.5	–49.3 G	–	31.0	0.02	475	1.06
	″	2	2	377 G	–35	–4.1	–	–	–	6.6	n.a.	214	1.0
	″	3	3	360	–34	–5.5	–	–	–	8.6	0.70	–	–
	″	3	2	354	–33	–2.3	–	–	–	3.9	0.63	–	–
	″	3	2	329	–29	–1.7	–	–	–	2.9	0.67	–	–
29/01	Quartz	1	3	392	–55	(397)	–	–	–	47.1	1.09	355	1.0
	″	1	2	259	–56	(367)	–	–	–	44.0	1.19	2311	1.0
	″	1	6	276	–55	(360)	–	–	–	43.3	1.17	1776	1.0
	″	1	4	285	–55	(311)	–	–	–	39.0	1.11	–	–
	″	2	7	350 G	–31	–0.5	–58.1	27.5 G	8.3	0.9	0.28	493	3.1
	″	2	6	358 G	–31	–0.6	–57.7	31.0 G	8.2	1.1	0.42	734	4.2
	″	2	4	329 G	–26	–1.2	–57.4	28.7 G	8.6	2.1	0.30	471	3.9
	″	2	2	327 G	–29	–2.9	–57.2	29.3 G	7.9	4.8	0.32	486	4.1
	″	2	11	327 G	–30	–2.9	–57.2	28.8 G	7.9	4.8	0.31	469	4.0
	″	2	2	292 G	–31	–1.6	–56.6	–32.2 G	–	2.7	0.03	108	1.5
	″	3	3	359	–35	–4.9	–	–	–	7.7	0.69	–	–
	″	3	3	333	–37	–2.3	–	–	–	3.9	0.68	–	–
	″	3	3	333	–30	–2.8	–	–	–	4.7	0.69	–	–
	″	3	5	332	–30	–3.0	–	–	–	5.0	0.70	–	–
	″	3	18	331	–34	–4.1	–	–	–	6.6	0.73	–	–

Table 7. (Contd.)

Sample	Mineral	Type*	*n*	T_{hom}, °C	T_{eut}, °C	$T_{ice\ melt}$ (NaCl), °C	$T_{melt\ CO_2}$, °C	$T_{hom\ CO_2}$, °C	$T_{gas\ hydrate\ melt}$, °C	C_{salt}, wt % NaCl equiv ($CaCl_2$)	*d*, g/cm^3	*P*, bar	$(P_{H_2O} + P_{gas})/P_{H_2O}$
154/05	Calcite	3	3	231	–31	–0.5	–	–	–	0.9	0.83	–	–
	″	3	3	194	–30	–0.4	–	–	–	0.7	0.88	–	–
	″	3	3	177	–31	–0.5	–	–	–	0.9	0.90	–	–
	″	3	2	170	–28	–0.4	–	–	–	0.7	0.91	–	–
	″	3	3	150	–29	–1.2	–	–	–	2.1	0.94	–	–
	″	3	5	146	–35	–1.2	–	–	–	2.1	0.94	–	–
163/05	Quartz	1	3	611	–62	(154)	–	–	–	29.9	n.a.	–	–
						–29.2				(25.0)			
	″	1	5	346	–54	(442)	–	–	–	52.2	1.20	2488	1.0
	″	1	4	422	–53	(208)	–	–	–	32.3	0.91	–	–
	″	1	3	306	–50	(419)	–	–	–	49.6	1.21	2673	1.0
	″	1	3	312	–56	(323)	–	–	–	40.0	1.10	301	1.0
	″	1	6	287	–54	(315)	–	–	–	39.4	1.12	596	1.0
	″	1	3	282	–61	(313)	–	–	–	39.2	1.12	649	1.0
	″	1	3	289	–55	(307)	–	–	–	38.7	1.11	404	1.0
	″	1	3	283	–53	(277)	–	–	–	36.6	1.09	–	–
	″	1	3	269	–55	(248)	–	–	–	34.6	1.09	–	–
	″	2	3	502 G	–47	–16.3	–56.7	25.2 G	–	19.7	0.25	1040	1.6
	″	2	3	473 G	–35	–14.6	–57.2	–0.4 G	–	18.3	0.10	657	1.3
	″	2	2	440 G	–44	(170)	–56.7	20.1 G	–	30.5	0.20	666	1.7
						–13.8				17.6			
	″	2	4	332 G	–30	–5.6	–57.2	–6.0 G	–	8.7	0.08	217	1.7
	″	2	2	317 G	–28	–5.9	–57.1	26.6 G	8.0	9.1	0.26	395	3.8
	″	3	4	438	–35	–4.4	–	–	–	7.0	0.47	–	–
	″	3	2	356	–61	–24.6	–	–	–	(23.2)	0.89	–	–
	″	3	3	348	–50	–17.2	–	–	–	(20.4)	0.88	–	–
	″	3	4	347	–34	–0.8	–	–	–	1.4	0.60	–	–
	″	3	5	336	–32	–1.3	–	–	–	2.2	0.64	–	–
	″	3	6	331	–50	–19.1	–	–	–	(20.7)	0.91	–	–
	″	3	3	314	–35	–5.5	–	–	–	8.6	0.79	–	–
	″	3	3	308	–40	–1.2	–	–	–	2.1	0.70	–	–
	″	3	3	273	–22	–1.0	–	–	–	1.7	0.77	–	–

* Fluid type: (1) brine, (2) gas, (3) solution.
n, number of inclusions; G, homogenization into gas; n.a., not analyzed.

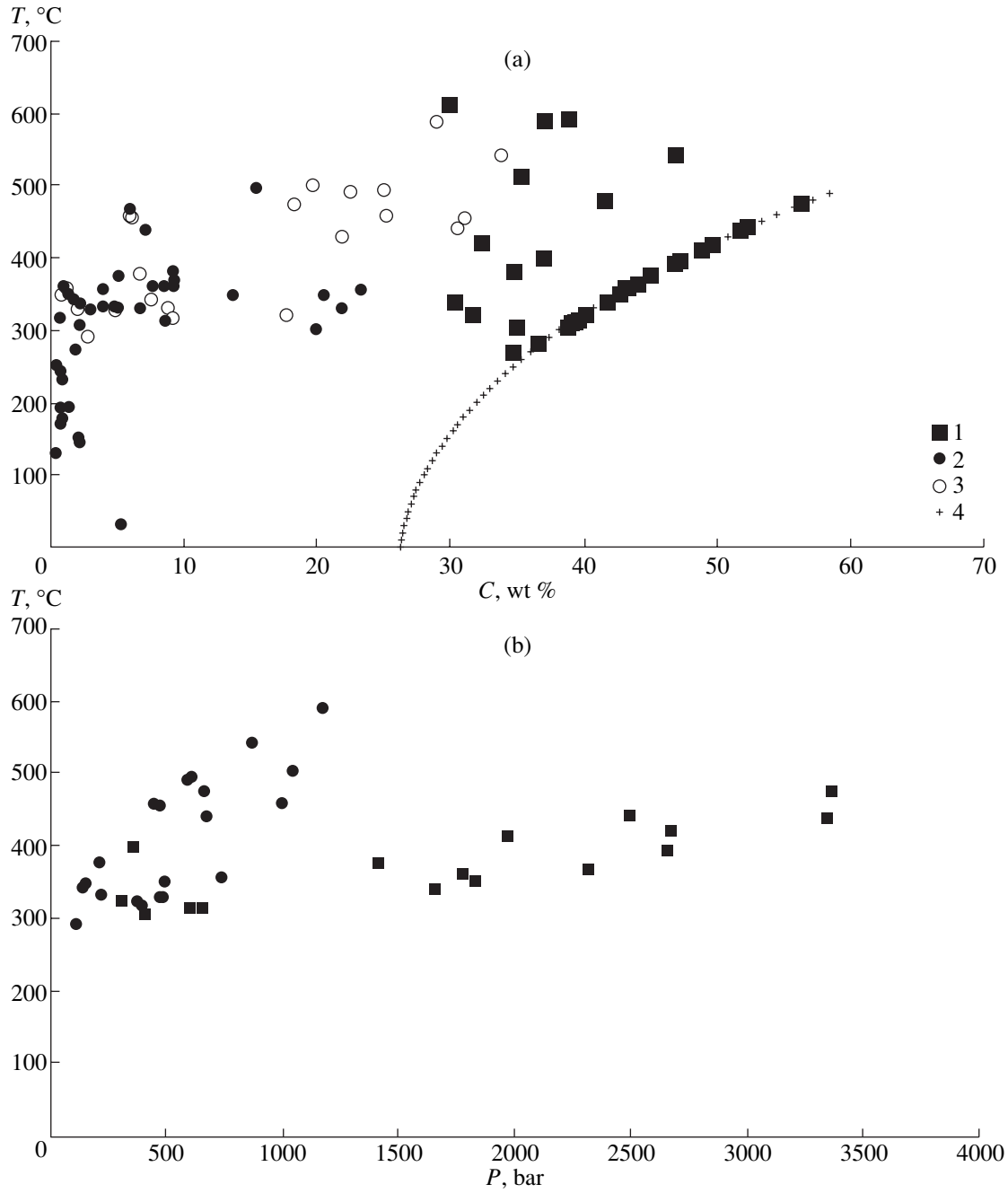

Fig. 16. (a) Temperature vs. salt concentration and (b) temperature vs. pressure for different types of ore-forming fluids at the Talatui deposit. (1) Brine, (2) diluted solution, (3) gas, (4) saturation curve in the H_2O–NaCl system.

$[NaMg_3Al_6(BO_3)_3Si_6O_{18}(OH)_4]$ were taken from (Garofalo et al., 2000). Activity coefficients of solutions were calculated from the Debye–Hückel equation in the second approximation (Helgeson et al., 1981).

The salt background of the initial fluid was set by NaCl and KCl concentrations: m_{NaCl} = 5 mol kg^{-1} and m_{KCl} = 2 mol kg^{-1} (Table 9). The concentrations of dissolved CO_2 and CH_4 in calculations were accepted equal to m_{CO_2} = 1 mol kg^{-1} and m_{CH_4} = 0.02 mol kg^{-1} (Table 9). Boron was introduced into the system as boric acid $[B(OH)_3]$ in concentrations varying from 0.1 to 5 mol kg^{-1}.

The objective of the modeling was to establish the maximum concentrations of ore elements in the fluid in various physicochemical settings corresponding to the evolution of ore-forming fluid at the Talatui deposit. For this purpose, excess initial amounts of Au, Ag, and Cu were set in the system to saturate the model solution with respect to these elements at any computational

Table 8. Bulk chemical composition of the material filling fluid inclusions in quartz from the Talatui deposit

Element	30/01	4208TL	3TL/85	163/05
		g/kg H_2O		
CO_2	10.47	49.75	16.20	15.28
CH_4	0.078	0.327	0.350	0.024
Cl^-	108.33	71.83	84.74	166.68
HCO_3^-	50.00	56.643	83.495	0.54
SO_4^{2-}	n.d.	n.d.	n.d.	66.23
Na	52.03	36.715	54.51	47.94
K	20.45	24.77	27.71	31.02
Ca	18.13	11.50	11.05	40.31
Mg	2.66	2.249	0.942	1.427
		mg/kg H_2O		
Br	480	37.2	189	1727
As	376	151	240	623
Li	62.81	24.2	43.9	34.2
B	1484	163	107	220
Rb	120	67.3	91.8	195.5
Cs	14.4	15.4	29.3	93.1
Sr	1386	381	253	1201
Mo	0.7	2.6	11.5	1.8
Ag	2.6	n.d.	0.28	0.14
Sb	4.9	6.9	5.7	36.1
Cu	166	178	181	101
Zn	2277	945	926	2019
Cd	7.7	7.8	5.2	15.8
Pb	62.4	7.4	22.6	38.7
Bi	0.07	0.07	0.28	0.34
Th	0.25	0.16	0.20	n.d.
U	1.0	0.23	0.04	0.02
Ga	1.14	1.49	1.37	2.28
Ge	0.99	1.45	2.64	1.68
Sc	11.9	21.16	71	50
Ti	20.2	7.55	26.6	13.6
Mn	4445	1894	1861	5754
Fe	794	1052	813	294
Co	2.09	1.12	3.6	0.81
Ni	17.3	9.8	12.4	11.8
Cr	n.d.	7.2	6.8	0.8
Y	0.33	0.04	0.09	0.04
Zr	1.4	0.18	0.9	0.23
Nb	0.01	0.05	0.21	n.d.
Sn	n.d.	n.d.	2.7	0.5
Ba	1307	189	136	578
W	0.48	0.07	6.90	12.3
Au	n.d.	0.42	n.d.	0.29
Hg	0.32	0.47	″	1.26
Se	n.d.	6.1	″	3.4
Tl	3.3	1.7	3.3	6.6
ΣREE	0.7	0.3	1.9	0.1
Hf	0.01	n.d.	n.d.	0.01

Note: n.d., not detected.

Table 9. Main parameters and results of thermodynamic modeling

T, °C	500	450	380	380
P, bar	2270	523	271	264
C_{salt}, wt %	41	41	41	7
C_{salt}, M	NaCl = 5; KCl = 2	NaCl = 5; KCl = 2	NaCl = 5; KCl = 2	NaCl = 0.9; KCl = 0.3
C_{CO_2}, M	1	1	1	0.18
C_{CH_4}, M	0.02	0.02	0.02	0.004
Phase state	One-phase region H_2O_{liq}	Two-phase region H_2O_{liq}/H_2O_{gas}	Two-phase region H_2O_{liq}/H_2O_{gas}	Two-phase region H_2O_{liq}/H_2O_{gas}
Calculated mineral assemblage	Anorthite	Anorthite		
	Dravite	Dravite	Dravite	Dravite
	Epidote	Epidote	Epidote	Epidote
	Orthoclase	Orthoclase	Orthoclase	
	Phlogopite	Phlogopite	Phlogopite	Phlogopite
				Talc
	Albite	Albite	Albite	Albite
	Pyrite	Pyrite	Pyrite	Pyrite
	Pyrrhotite	Pyrrhotite	Pyrrhotite	Pyrrhotite
	Magnetite	Magnetite	Magnetite	Magnetite
	Tremolite	Tremolite	Tremolite	Tremolite
	Quartz	Quartz	Quartz	Quartz
m_{Au}, mol/kg	1.02×10^{-5}	4.63×10^{-6}	7.48×10^{-7}	6.79×10^{-7}
Main species, Au, mol %	$AuCl_2^-$, 64.1	$AuCl_2^-$, 37.0	$AuCl_2^-$, 12.6	$AuCl_2^-$, 0.7
	$Au(HS)_2^-$, 21.2	$Au(HS)_2^-$, 31.5	$Au(HS)_2^-$, 26.2	$Au(HS)_2^-$, 27.7
	AuHS, 13.9	AuHS, 30.5	AuHS, 59.6	AuHS, 69.8
m_{Ag}, mol/kg	1.32×10^{-2}	1.11×10^{-2}	3.16×10^{-3}	1.55×10^{-4}
Main species, Ag, mol %	$AgCl_2^-$, 99.8	$AgCl_2^-$, 99.9	$AgCl_2^-$, 99.9	$AgCl_2^-$, 99.3
m_{Cu}, mol/kg	2.3×10^{-2}	7.44×10^{-3}	1.73×10^{-3}	9.31×10^{-5}
Main species, Cu, mol %	$CuCl_2^-$, 99.4	$CuCl_2^-$, 99.4	$CuCl_2^-$, 99.4	$CuCl_2^-$, 89.7
				CuHS, 10.1
pH	4.67	5.63	5.28	5.40
Shift*	–0.49	–0.40	–0.54	–0.42
Eh (B)	–0.68	–0.75	–0.63	–0.65
I (mol kg^{-1})	2.08	1.62	2.73	0.51
$\log f_{O_2}$	–21.17	–23.68	–27.78	–27.78
$\log f_{CO_2}$	1.65	1.40	1.61	0.85
$\log f_{H_2S}$	0.84	0.17	–0.35	–0.30
$\log f_{B(OH)_3}$	0.73	–0.12	–0.88	–0.84

* Shift (in pH units) toward the acid region relative to the neutral point.

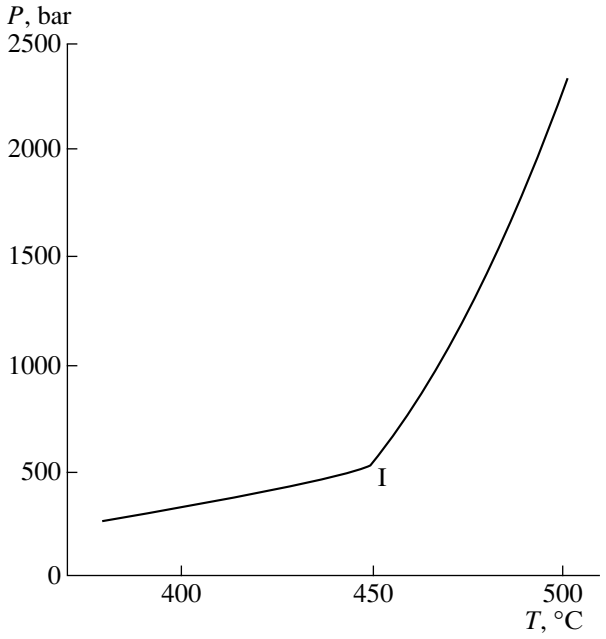

Fig. 17. Variation in temperature and pressure of the model fluid (m_{NaCl} = 5 mol kg^{-1}, m_{KCl} = 2 mol kg^{-1}, m_{CO_2} = 1 mol kg^{-1}) accepted in this study. I is the point of liquid–vapor equilibrium at 450°C.

PTX point. It should be noted that many aspects of the behavior of gold in a similar system were considered by Heinrich (2005). Therefore, we focused our efforts largely on the joint behavior of Au, Ag, and Cu in the ore-forming system.

The *PT* parameters of the system set in computations were intended to clarify the effects of different factors on the transport properties of ore elements. In accordance with the progressive variation of physicochemical parameters discussed above, the following scenario of ore fluid evolution has been accepted. The initially hot (T = 500°C) and dense (ρ = 1.077 g cm^{-3}) fluid at P = 2270 bar cooled, remaining a closed system. The drop in temperature and pressure, being bound by the condition of constant fluid density, proceeded along the chosen isochore ρ = 1.077 g cm^{-3} (Fig. 17). The point of two-phase equilibrium was reached at 450°C and P = 523 bar, and the further decrease in temperature occurred along the curve of water–salt fluid boiling (Fig. 17). The *PT* parameters of the fluid that correspond to this scenario were computed from equations of state (Anderko and Pitzer, 1993; Duan et al., 1995) with use of a program package (Bakker, 2003).

In addition, the effects that accompanied boil-off of fluids at a constant temperature (T = 380°C) were investigated. The isothermic boiling was modeled as follows. The initial partial pressures (P) of all volatile components (H_2O, CO_2, CH_4, H_2S, and $B(OH)_3$) on the assumption of ideal gas behavior were calculated first for the initial fluid on the curve of two-phase equilibrium. Afterward, the amount of H_2O in fluid was diminished by a certain value, and the concentration of volatiles was decreased as well proportionally to the ratio of the pressure of a volatile to the sum of partial pressures of all volatile components. For example, the computation for our fluid at 380°C gave P_{H_2O} = 113.8 bar, P_{CO_2} = 40.8 bar, and P_{H_2S} = 0.45 bar, while the sum of partial pressures of volatiles is 155.2 bar. Thus, the mole fractions of the gas species in equilibrium with the liquid solution were x_{H_2O} = 113.8/155.2 = 0.733, x_{CO_2} = 40.8/155.2 = 0.263, and x_{H_2S} = 2.87 × 10^{-3}. Therefore, it was accepted that, when 0.733 mol H_2O had been boiled off, the dense fraction of fluid was depleted in CO_2 by 0.263 mol and in H_2S by 2.87 × 10^{-3} mol. After introduction of the corresponding changes to the fluid composition, the equilibrium was calculated after the first stage of boil-off. The result obtained gave an estimate of the equilibrium partial pressures of volatile components, which was used further in modeling boil-off of the next small portion of dissolvent.

The equilibrium mineral assemblage obtained from the computations (quartz–anorthite–epidote–potassium feldspar–phlogopite–tremolite–albite) fits that observed in the ore and remains virtually unchanged at all temperatures (Table 9). Only at T < 430°C does anorthite become unstable, being converted into epidote. As was mentioned above, the oxygen and hydrogen sulfide fugacities in the system are controlled by the Py–Po–Mt buffer and vary (on logarithmic scale) from –21.17 at 450°C to –27.78 at 380°C for O_2 and from 0.84 at 450°C to –0.35 at 380°C for H_2S. At a high initial concentration of boric acid (>0.4 mol kg^{-1}), dravite is stable in the system, whereas schorl is far from saturation. The pH of the fluid first grows and then somewhat drops with the temperature decrease, from 4.67 at 450°C to 5.66 at 420°C and then to 5.28 at 380°C. Thereby, the fluid remains slightly acid, while the pH shift relative to the neutral point remains almost unchanged and equals ~0.5 unit. The solubilities of Au, Ag, and Cu are controlled by the presence of native gold (Au_{cr}), acanthite (Ag_2S), and chalcopyrite ($CuFeS_2$), respectively.

The relationships of the maximum concentrations of ore elements in the system versus temperature are shown in Fig. 18a. It can be seen that, if the gold concentration decreases monotonically during cooling, the solubility of silver reaches a maximum in the region corresponding to movement along the curve of saturated vapor of the water–salt fluid. The curve for copper occupies a transitional position with a slight increase in solubility at 420–440°C. Such a behavior of solubility of ore elements is determined by their speciation in solution and by the composition of the minerals that

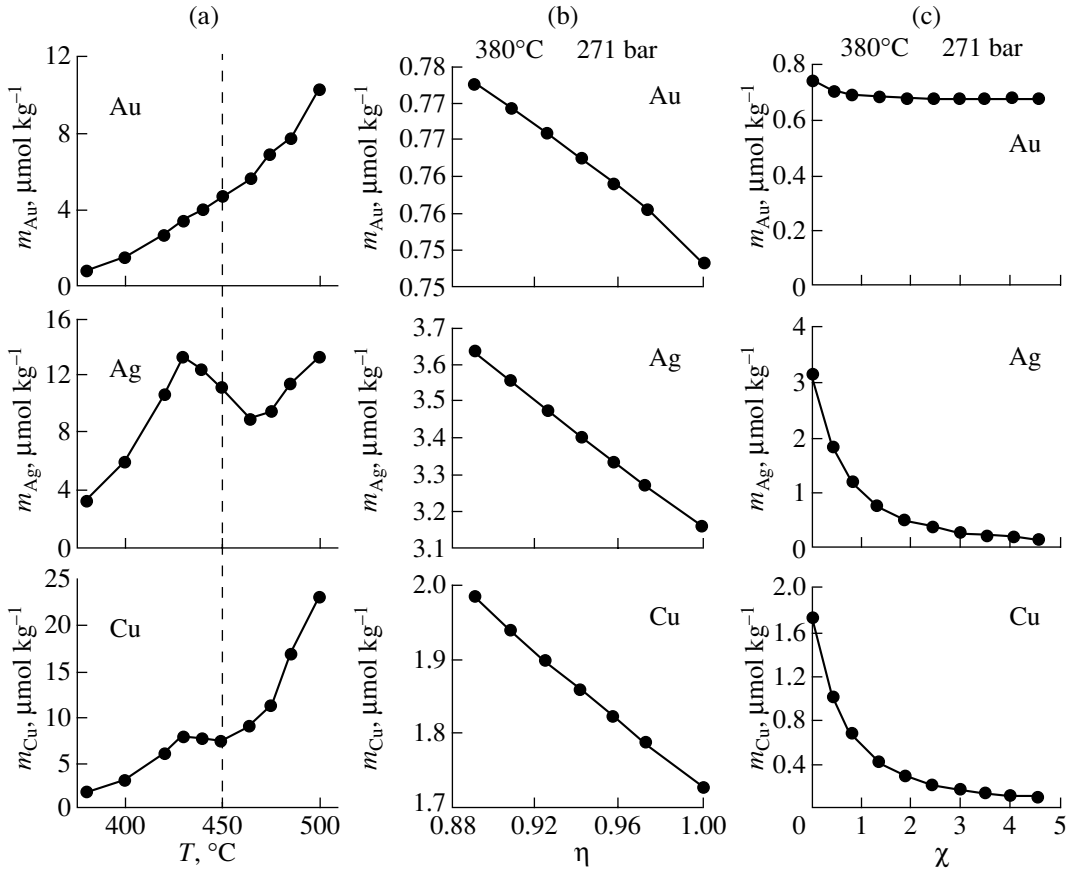

Fig. 18. Solubility of Au, Ag, and Cu as a function of (a) temperature (according to the scenario accepted in this study; the vertical dashed line at 450°C corresponds to the two-phase equilibrium during evolution of water–salt fluid); (b) degree of fluid boil-off (η); and (c) degree of fluid dilution (χ).

control the solubility of these elements. As concerns the behavior of gold at $T < 450$°C, the pivotal reaction is

$$Au_{cr} + 3.5H_2S^0 + 0.5Mag \longleftrightarrow Au(Hs)_2^- + H^+ + 1.5Po + 2H_2O, \quad (1)$$

so that the monotonic decrease in the concentration of dissolved hydrogen sulfide (H_2S^0) with temperature that is determined by the Py–Po–Mt buffer gives rise to a corresponding decrease in the concentration of the prevalent gold complex [$Au(HS)_2^-$]. Silver occurs in solution largely as $AgCl_2^-$, and the corresponding dissolution reaction is

$$Ag_2S + 2H^+ + 4Cl^- \longleftrightarrow 2AgCl_2^- + H_2S^0. \quad (2)$$

In this case, the decrease in the concentration of H_2S^0 shifts the reaction equilibrium to the right, raising Ag solubility. In addition, the decrease in temperature upon movement of a data point along the curve of saturated vapor at $T < 450$°C is accompanied by an increase in dissociation of NaCl and KCl. The latter circumstance leads to enrichment in free Cl^- and thus to the shift of reaction (2) toward its products. Similarly, the reaction of Cu dissolution is written as

$$CuFeS_2 + 2Cl^- \longleftrightarrow CuCl_2^- + Py, \quad (3)$$

so that the aforementioned increase in Cl^- molality in solution also promotes some growth of copper solubility in fluid.

Such a difference in the behavior of gold and silver may serve as a cause of precipitation of gold of a high fineness within the temperature range 460–420°C. It should be emphasized that the maximum Ag and Cu concentrations are three orders of magnitude higher than the Au concentration in fluid.

It should also be noted that the prevalent speciation of gold depends on temperature. If at <450°C most gold occurs in solution as a hydrosulfide complex, then at 500°C only 25% of the metal is contained in such a complex, while the remainder (75%) is transported as chloride complexes.

The variation of total boron content in the system virtually does not affect the concentration of ore elements in fluid. Thus, at 450°C, the maximum B concentration equals 0.295 mol kg^{-1} and is controlled by the

solubility of dravite at this temperature. Thereby, the Au, Ag, and Cu concentrations are 4.63×10^{-6}, 1.11×10^{-2}, and 7.44×10^{-3} mol kg^{-1}, respectively. The depletion of B down to 0.1 mol kg^{-1} leads to only an insignificant change in the molality of ore elements (in the same sequence): 4.87×10^{-6}, 1.26×10^{-2}, and 8.42×10^{-3} mol kg^{-1}.

The effect of isothermic boiling of fluid is illustrated in Fig. 18b. The degree of boil-off η is plotted on the abscissa axis as the ratio of the amount of water left in the fluid n_{H_2O} to its initial amount $n^0_{H_2O}$: $\eta \equiv n_{H_2O}/n^0_{H_2O}$. Thus, $\eta = 1$ corresponds to the onset of boiling, whereas the decrease in η characterizes the amount of the fluid that has been boiled off. As previously, the maximum concentrations of ore elements in the dense fraction of the fluid are plotted on the ordinate. It is seen that boil-off promotes an insignificant increase in the solubility of all ore elements. In terms of the model used, the removal of such volatiles as CO_2, $B(OH)_3$, and CH_4 practically does not affect the equilibrium solubilities of Au, Ag, and Cu. At the same time, the concentrations of ligands change insignificantly: the HS^- concentration is maintained virtually constant by the Py–Po–Mt buffer and the molality of Cl^- ion somewhat increases owing to the drop in the amount of dissolvent. The latter circumstance is a cause of the aforementioned increase in solubility of ore components. This effect is more distinct for Ag and Cu because leading dissolution reactions (2) and (3) proceed with the participation of chloride complexes.

As was mentioned above, the data on fluid inclusions testify to the dilution of ore fluid with low-mineralized meteoric water at the late stage of the process. To estimate the effect of such dilution, the solubility of ore components was computed depending on the amount of pure dissolvent (H_2O) added to the system at constant temperature (380°C) and pressure (271 bar). The ratio of the amount of newly supplied water n_{H_2O} to the amount of water in the initial fluid

$$n^0_{H_2O}: \chi \equiv n_{H_2O}/n^0_{H_2O}$$

was used as a parameter characterizing the degree of dilution. The dependence of the equilibrium concentration of ore elements on χ is shown in Fig. 18c. As can be seen, the supply of low-mineralized water decreases the solubility of ore elements. However, while the solubility of Au decreases insignificantly, the solubility of Ag and Cu falls by more than an order of magnitude at $\chi > 5$. This difference is determined by the dissolved species of elements and the composition of minerals controlling their solubility. For Ag and Cu, this is chloride complexes, so that dilution of the fluid, diminishing the concentration of the ligand Cl^-, shifts the equilibrium of reactions (2) and (3) to the left. The contribution of the chloride complex to the total Au concentration in solution at 380°C does not exceed 13%, while the concentration of the ligand HS^-, determining the prevalent species [$AuHS^0$] and [$Au(HS)_2^-$] in solution, remains practically constant owing to the Py–Po–Mt buffer. Such effects may be a cause of ore element separation during the evolution of hydrothermal fluids.

DISCUSSION

The results of mineralogical and thermobarogeochemical studies of ore at the Talatui deposit and thermodynamic modeling allow us to reconstruct the general physicochemical process of ore deposition, which started with the escape of a high-temperature chloride solution from a parental intrusion and interaction of this solution with country gabbroic rocks at a high temperature. The granite and granite porphyry dikes that crop out at the deposit obviously could not have provided the necessary heating, and therefore a shallow parental intrusion of larger dimensions is suggested. During cooling from 600 to 400°C, highly concentrated chloride brine periodically boiled up and coexisted with the gas phase under conditions of abruptly changing pressure controlled by faulting. In other words, boiling off of fluid near a heat source occurred and the concentrations of ore components therein increased (White et al., 1971; Kigai, 1979). The hydrothermal activity at this stage was accompanied by brittle failure (fracturing) of the host rocks; hydraulic failure could have developed as well. The solubility of Au and Ag in the concentrated chloride solution was rather high at this stage. The temperature drop led to decreasing solubility of Au and its precipitation in native form, whereas the solubility of Ag did not decrease and this metal remained in the solution. Early mineral assemblages bearing native gold of a high fineness—a magnetite–epidote–actinolite–quartz–feldspar assemblage with biotite, tourmaline, scheelite, and wolframite, as well as a pyrite–magnetite–tourmaline–quartz assemblage—were formed at this stage.

Further opening of fractures and mass boiling of fluid resulted in precipitation of a chalcopyrite–molybdenite assemblage with sphalerite, linnaeite, glaucodot, chlorite, carbonate, and quartz.

An abrupt decrease in salt concentration in the fluid was probably related to the development and complication of a fracture system, the arising of a convective hydrothermal system above the parental intrusion, and the involvement of low-mineralized meteoric water in this process. The decreased salt concentration in solution led to a decrease in Ag and Bi solubility and precipitation of some amount of bismuth and silver tellurides and sulfides. However, the bulk of Au, Ag, Bi, and other components was removed in the course of convection to the upper portion of the ore system, forming ore mineralization of the Darasun type. Precisely such a line of evolution could have led to the limited devel-

Table 10. Sulfur, oxygen, and carbon isotopic compositions of minerals from the Talatui deposit and calculated oxygen isotopic composition of water and carbon isotopic composition of CO_2 in fluid

Sample	Mineral	$\delta^{34}S$, ‰ (CDT)	$\delta^{18}O$, ‰ (SMOW)	$\delta^{13}C$, ‰ (PDB)	T, °C	$\delta^{18}O_{H_2O}$, ‰	$\delta^{13}C_{CO_2}$, ‰
30/01	Tourmaline	n.a.	+7.6	n.a.	550	+7.7	n.a.
146/05	Carbonate	〃	+15.7	–5.2	270	+9.2	–14.8
144/05	〃	〃	+12.5	–4.9	250	+5.2	–16.1
140/05	〃	〃	+12.4	–3.9	250	+5.1	–15.1
165/05	〃	〃	+12.3	–3.9	240	+4.6	–16.0
154/05	〃	〃	+9.9	–5.3	180	–0.8	–24.9
3Tl85	〃	〃	+6.2	–7.1	130	–8.0	–36.8
49/32a	〃	〃	+6.0	–3.4	110	–10.1	–38.7
141/05	Pyrite	–0.1	n.a.	n.a.	n.a.	n.a.	n.a.
142/05	〃	+1.58	〃	〃	〃	〃	〃
145/05	〃	+0.4	〃	〃	〃	〃	〃
147/05	〃	–0.22	〃	〃	〃	〃	〃
147/05a	〃	–0.39	〃	〃	〃	〃	〃
147/05	〃	+0.5	〃	〃	〃	〃	〃
159/05	〃	–0.1	〃	〃	〃	〃	〃
163/05	〃	+0.38	〃	〃	〃	〃	〃
163/05a	〃	+0.6	〃	〃	〃	〃	〃
29/01	〃	+0.1	〃	〃	〃	〃	〃
28/01	〃	+4.6	〃	〃	〃	〃	〃
23/01	〃	0.4	〃	〃	〃	〃	〃
140/05	Chalcopyrite	–0.06	〃	〃	〃	〃	〃
140/05a	〃	0.4	〃	〃	〃	〃	〃
141/05	〃	+0.93	〃	〃	〃	〃	〃
142/05	〃	+1.50	〃	〃	〃	〃	〃
147/05	〃	–1.67	〃	〃	〃	〃	〃
153/05	〃	–1.90	〃	〃	〃	〃	〃
3Yu	〃	–0.1	〃	〃	〃	〃	〃

Note: n.a., not analyzed.

opment of medium- and low-temperature assemblages at the Talatui deposit and the good preservation of the early high-temperature mineral assemblages with native gold of high fineness. At the same time, such a model does not conflict with existing differences in mineral composition of gold deposits in the Darasun ore district.

The ore deposition was completed with the formation of bornite, carbonate, and quartz.

This model is consistent with the previously stated opinion (Yurgenson and Yurgenson, 1995; Prokof'ev et al., 2005b) that the ore at the Talatui deposit was formed in the deep portion of a Darasun-type ore-forming system. The finds of Bi sulfosalts (Prokof'ev et al., 2005a) and Ag tellurides and sulfosalts at the Talatui deposit testify to genetic links between the Talatui and Darasun deposits.

At the same time, the question of the economic type of the Talatui deposit arises. Comparison of its mineral composition with the known types of gold deposits shows that the Talatui deposit may be regarded as an analogue of the chalcopyrite–molybdenite (Nekrasov, 1991) or porphyry gold (Safonov, 1997) type of ore mineralization. The occurrence of propylitic wall-rock alteration, abundant magnetite, an Au-bearing chalcopyrite–molybdenite assemblage, gold of high fineness in early mineral assemblages, sulfates contained in ore, and vague orebody boundaries—all this is consistent with the main attributes of porphyry copper deposits (Popov, 1977; Titley and Bean, 1981; Sillitoe, 2000). It should be noted that Stolyarov (1992) was the first to suggest, based on finds of anhydrite microinclusions in quartz, the porphyry type of the Talatui deposit. Our data on the formation conditions of this deposit and the

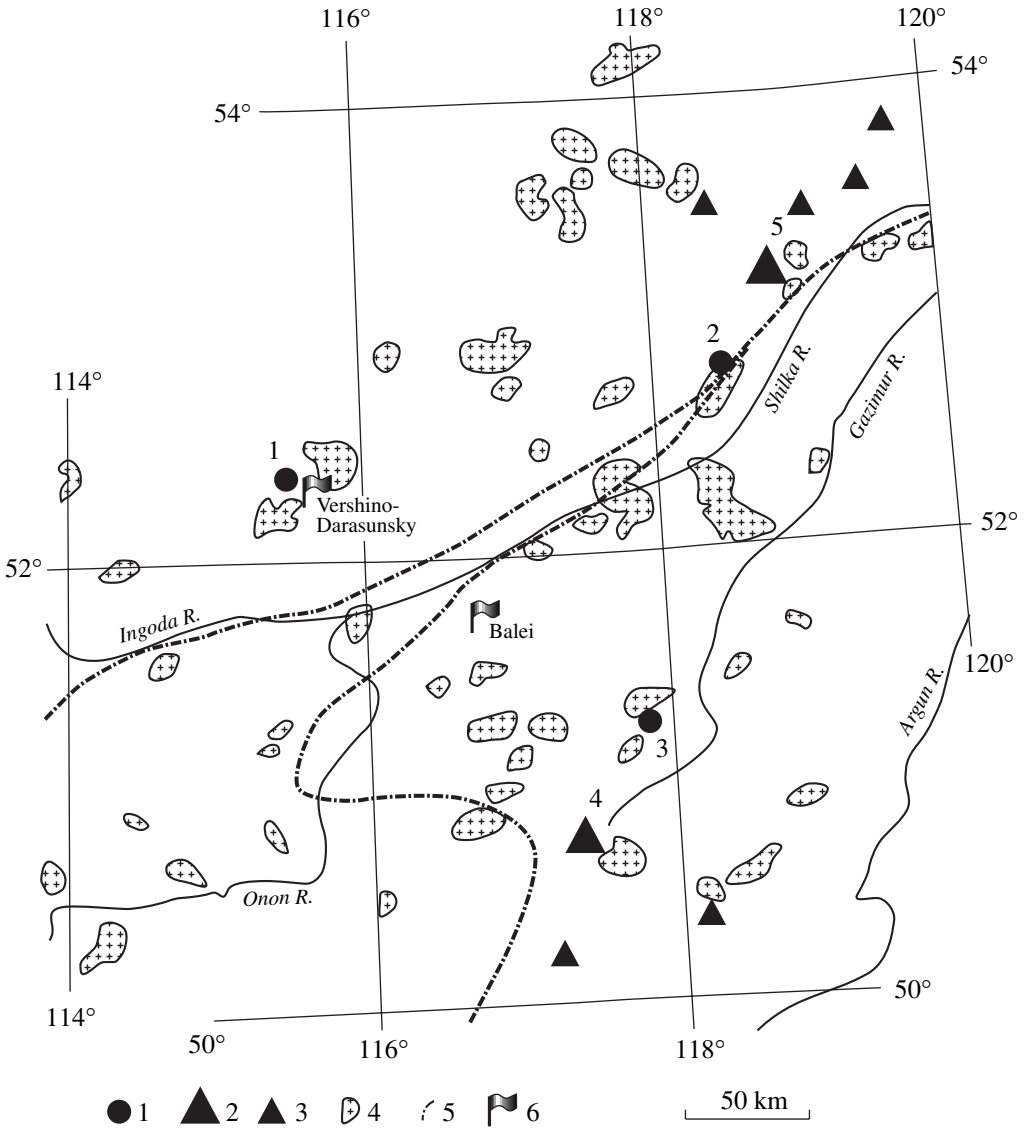

Fig. 19. Location of high-temperature porphyry gold and porphyry copper deposits in the central Mongolia–Okhotsk Belt. (1–3) Deposits: (1) porphyry gold, (2) large porphyry copper, (3) small porphyry copper, after Sotnikov (2005); (4) Middle–Late Jurassic minor porphyry intrusions of K-rich granitoids; (5) large faults; (6) settlements. Deposits (numerals in map): (1) Talatui, (2) Kariisky, (3) Bugdaya, (4) Shakhtama, (5) Zhireken.

results of a fluid inclusion study that indicate a high temperature of the onset of ore formation, boiling of fluid, and capturing of chloride brines also testify to similarity of the ore-forming process at the Talatui deposit with *PTX* parameters at typical porphyry copper and high-sulfidation deposits (Roedder, 1971; Nash, 1976; Chivas and Wilkins, 1977; Eastoe, 1978; Ahmad and Rose, 1980; Bloom, 1981; Ruggieri et al., 1997; Wang et al., 1999; Harris et al., 2005; Frikken et al., 2005). Many mineralogical and geochemical features (the proportions of Au and Cu in ore, the high Re content in molybdenite, and the character of metasomatic alteration) of the Talatui deposit are similar to those at porphyry gold–copper deposits (Krivtsov et al., 1986). The short distance between separate deposits of the Darasun ore district, as well as the genetic and chronological links with similar igneous rocks, allow their evolution to be regarded in terms of a common fluid–magmatic system of porphyry type (Prokof'ev et al., 2000). The Talatui deposit was formed against the background of boil-off (heterogenization) of chloride fluids close to a magma chamber. The K/Rb (170–368), Sr/Rb (2.8–11.5), Ba/Rb (1.5–10.9), Sr/Ba (1.1–2.0), and Ni/Co (3.4–8.8) ratios in fluid inclusions are close to the corresponding values in granitic systems (Irber, 1999). The oxygen isotopic composition of tourmaline and carbonates (Table 10) indicates that $\delta^{18}O$ of aqueous ore-forming fluid pertaining to the early mineral assemblages is 4.6–9.2‰ and, according to the existing classifications (Sheppard, 1986; Kyzer, 1987), corre-

sponds to magmatic fluid. The value of $\delta^{18}O$ of the fluid responsible for the formation of younger carbonate is lower owing to the dilution of magmatic fluid with meteoric water. The enrichment of carbon dioxide in a light carbon isotope (Table 10) may be caused by redox reactions. The sulfur isotopic composition of sulfides is close to the meteoritic standard, as is typical of porphyry-type deposits (Lang et al., 1989). According to the modern concept (Cox and Singer, 1992), porphyry gold–copper deposits are formed in marginal continental rift troughs. The new data on the age of the gold mineralization of the Darasun ore district are in good agreement with this interpretation because the Darasun deposit was formed in the Early Cretaceous during rifting of the Mongolia–Okhotsk Belt (Prokof'ev et al., 2006).

Porphyry copper deposits reveal a specific zoning of metasomatic alteration and ore mineralization (Lowell and Guilbert, 1970). The information on the zoning at the Talatui deposit remains insufficient. However, the mineral assemblages of metasomatic wall-rock rocks fit the potassic and propylitic alteration at porphyry-type deposits (Lowell and Guilbert, 1970; Popov, 1977). Propylitic alteration is commonly localized in the outer zones, with the exception of phlogopite-bearing propylites that replace basic rocks (as takes place at the Talatui deposit), where propylites are located in the intermediate zone. Potassic alteration with orthoclase is typical of inner zones. Ore zone 3 at the Talatui deposit, which is composed of orthoclase- and phlogopite-bearing metasomatic rocks, was formed at a higher temperature and closer to the center of the ore-forming system than ore zone 2, with chalcopyrite and a high Au grade. This general pattern should be specified further by detailed mapping of ore and metasomatic zoning.

At the same time, some features of the ore composition at the Talatui deposit distinguish it from typical porphyry deposits and suggest a similarity with skarn-related gold deposits. In particular, this similarity is supported by a relatively high scheelite content in ore and an abundance of Ca and Te minerals, probably, owing to the predominance of gabbroic host rocks enriched in calcium and tellurium.

It should be noted that some other deposits similar to Talatui are known in the Transbaikal region, for example, an actinolite–magnetite type of gold ore at the Novinka deposit in the Kariisky ore district. The fluid regime of the formation of this deposit has much in common with that of Talatui (Prokof'ev et al., 1997): the ore formation started at 575°C, and the salt concentration was higher than 50 wt %. The porphyry-type gold–copper deposits of the eastern Transbaikal region are spatially related to fields of minor porphyry intrusions of elevated alkalinity and are controlled by linear tectonic zones (Fig. 19) that bound plates (Zorin et al., 2001). The geodynamic position of porphyry copper deposits above plunging plates has long been known (Sillitoe, 1972). Since the gold deposits of the Darasun type in the Transbaikal region belong to the group of porphyry gold–copper deposits, geodynamic criteria may be used for their prospecting. The proposed identification of the Tulatui deposit as a porphyry-type object necessitates its reappraisal on the basis of new criteria, as this may increase the value of the deposit owing to detection of additional ore components and the improvement of ore processing technology. In particular, it is necessary to examine the Re distribution in ore in terms of its possible recovery.

The new data on the formation conditions of the Talatui deposit provide insights into the overall ore zoning of the Darasun ore district and show that the style of ore mineralization changes with depth. The high-temperature phlogopite-bearing propylites as products of metasomatic wall-rock alteration at the Talatui deposit differ from the premineral propylites at the Teremki and Darasun deposits. Therefore, it is necessary to delineate the metasomatic zones closely related to ore formation throughout the Darasun ore district. The results obtained may be helpful for planning further geological exploration and choosing an optimal ore processing technology at the Talatui deposit.

CONCLUSIONS

The chemical and mineral compositions of ore from the Talatui gold deposit in the eastern Transbaikal region have been studied. Some previously unknown minerals have been identified: ilmenite, siegenite, glaucodot, wittichenite, matildite, hessite, pilsenite, zircon, tremolite, cummingtonite, hercynite, and goethite. A high Re content has been detected in molybdenite.

The spatial separation of gold and silver at the deposit is caused by different mineral species of these elements and their diachronous precipitation during the ore-forming process. Gold crystallized along with the early mineral assemblages, beginning from virtually pure gold with a fineness of 996. Silver precipitated largely at the end of the process as hessite and matildite.

The main parameters of ore deposition have been determined: a temperature of 610–145°C, a pressure of 3370–110 bar, and a salt concentration ranging from 56.3 to 0.4 wt % NaCl equiv. A heterogeneous state (boiling) of fluid at the early stages has been documented. The elemental and isotopic composition of fluid testifies to its magmatic origin and confirms the participation of meteoric water at the late stage of ore formation.

Thermodynamic modeling reproduces the main specific features of ore formation and explains the spatiotemporal separation of Au and Ag in the ore-forming process.

On the basis of several attributes, the Talatui deposit has been referred to the porphyry gold–copper economic type. The specific features of the mineral composition of ore are caused by the localization of ore mineralization in basic host rocks.

A physicochemical model of the gold mineralization in the Darasun ore district has been proposed.

ACKNOWLEDGMENTS

We thank V.P. Unzhakov, G.N. Stakheev, and Yu.A. Alferov (geologists of the Darasun Mine) for their assistance in studying the deposit. We are also grateful to N.N. Kononkova, I.A. Bryzgalov, L.P. Nosik, V.I. Ustinov, S.G. Kryazhev, and Yu.V. Vasyuta for performing analyses. This study was supported by the Russian Foundation for Basic Research, project nos. 04-05-65119 and 04-05-64407.

REFERENCES

1. S. N. Ahmad and A. W. Rose, "Fluid Inclusions in Porphyry and Skarn Ore at Santa Rita, New Mexico," Econ. Geol. **75**, 229–250 (1980).
2. N. N. Akinfiev, "Algorithm for Computation of Heterogeneous Equilibria Using Microcomputers," Geokhimiya **24** (6), 882–890 (1986).
3. N. N. Akinfiev and A. V. Zotov, "Thermodynamic Description of Chloride, Hydrosulfide, and Hydroxocomplexes of Ag(I), Cu(I), and Au(I) at Temperatures of 25–500°C and Pressures of 1–2000 bar," Geokhimiya **39** (10), 1–17 (2001) [Geochem. Intern. **39** (10), 990–1006 (2001)].
4. N. N. Akinfiev, M. V. Voronin, A. V. Zotov, and V. Yu. Prokof'ev, "Experimental Study of Stability of Chlorborate Complex and Thermodynamic Description of Water Components in B–Na–Cl–O–H System to 350°C," Geokhimiya **44** (9), 937–949 (2006) [Geochem. Intern. **44** (9), 867–878 (2006)].
5. A. Anderko and K. S. Pitzer, "Equation-of-State Representation of Phase Equilibrium and Volumetric Properties of the System NaCl–H_2O above 573 K," Geochim. Cosmochim. Acta **57**, 1687–1680 (1993).
6. R. J. Bakker, "Package FLUIDS 1. Computer Programs for Analysis of Fluid Inclusion Data and for Modeling Bulk Fluid Properties," Chem. Geol. **194**, 3–23 (2003).
7. E. Bastrakov, Y. Shvarov, S. Girvan, et al., "FreeGs: Web-Enabled Thermodynamic Database for Modeling of Geochemical Processes," in *Proceedings of the 17th Australian Geol. Convention on Dynamic Earth: Past, Present and Future* (Hobart, 2004), No. 73.
8. B. I. Benevol'sky, *Gold of Russia* (Geoinformmark, Moscow, 2002) [in Russian].
9. M. S. Bloom, "Chemistry of Inclusion Fluids: Stockwork Molybdenum Deposits from Questa, New Mexico, and Hudson Bay Mountain and Endaco, British Columbia," Econ. Geol. **76**, 1906–1920 (1981).
10. R. J. Bodnar and M. O. Vityk, "Interpretation of Microthermometric Data for H_2O–NaCl Fluid Inclusions," in *Fluid Inclusions in Minerals: Methods and Applications* (Siena, Pontignano, 1994), pp. 117–130.
11. M. M. Boldyreva, A. M. Egorov, and O. A. Yakovleva, "Cobalt and Nickel Sulfides from the Udokan Deposit," Dokl. Akad. Nauk SSSR **286** (5), 1224–1227 (1986).
12. A. S. Borisenko, "Cryometric Analysis of Salt Composition in Gas–Fluid Inclusions in Minerals," Geol. Geofiz. **18** (8), 16–27 (1977).
13. S. S. Borishanskaya, R. A. Vinogradova, and G. A. Krutov, *Nickel and Cobalt Minerals (Classification, Description, and Diagnostics)* (Moscow State Univ., Moscow, 1981) [in Russian].
14. P. Brown, "FLINCOR: A Computer Program for the Reduction and Investigation of Fluid Inclusion Data," Am. Miner. **74**, 1390–1393 (1989).
15. D. P. Cox and D. A. Singer, "Mineral Deposit Models," US Geol. Surv. Bull., No. 1693 (1992).
16. Z. Duan, N. Möller, and J. H. Weare, "Equation of State for the NaCl–H_2O–CO_2 System: Prediction of Phase Equilibrium and Volumetric Properties," Geochim. Cosmochim. Acta **59**, 2869–2882 (1995).
17. C. J. Eastoe, "A Fluid Inclusion Study of the Pananguna Porphyry Copper Deposit, Bougainville, Papua New Guinea," Econ. Geol. **73**, 721–748 (1978).
18. P. H. Frikken, D. R. Cooke, J. L. Walshe, et al., "Mineralogical and Isotopic Zonation in the Sur-Sur Tourmaline Breccia, Rio Blanco–Los Bronces Cu–Mo Deposit, Chile: Implications for Ore Genesis," Econ. Geol. **100**, 935–961 (2005).
19. P. Garofalo, A. Audetat, D. Gunther, et al., "Estimation and Testing of Standard Molar Thermodynamic Properties of Tourmaline End-Members Using Data of Natural Samples," Am. Mineral. **85**, 78–88 (2000).
20. A. S. Harris, S. D. Golding, and N. C. White, "Bajo de la Alumbrera Copper–Gold Deposit: Stable Isotope Evidence for a Porphyry-Related Hydrothermal System Dominated by Magmatic Aqueous Fluids," Econ. Geol. **100**, 863–886 (2005).
21. F. C. Hawthorne and D. J. Henry, "Classification of Minerals of Tourmaline Group," Eur. J. Mineral. **11**, 201–215 (1999).
22. C. A. Heinrich, "The Physical and Chemical Evolution of Low-Salinity Magmatic Fluids at the Porphyry to Epithermal Transition: A Thermodynamic Study," Miner. Deposita **39**, 864–889 (2005).
23. H. C. Helgeson, D. H. Kirkham, and G. C. Flowers, "Theoretical Prediction of the Thermodynamic Behavior of Aqueous Electrolytes at High Pressures and Temperatures: IV. Calculation of Activity Coefficients, Osmotic Coefficients and Apparent Molal and Standard and Relative Molal Properties to 600 C and 5 Kb," Am. J. Sci. **281**, 1249–1516 (1981).
24. G. F. Il'ina, "Integration of Geological–Structural and Geochemical Methods for Large-Scale Forecasting of Mineralization at the Talatui Deposit (Eastern Transbaikal Region)," in *Proceedings of IV Joint International Seminar on Applied Geochemistry Dedicated to Academician L.V. Tauson* (Irkutsk, 1994), Vol. 1, pp. 178–179 [in Russian].
25. W. Irber, "The Lanthanide Tetrad Effect and Its Correlation with K/Rb, Eu/Eu*, Sr/Eu, Y/Ho, and Zr/Hf of Evolving Peraluminous Granite Suites," Geochim. Cosmochim. Acta **63** (3/4), 489–508 (1999).
26. J. W. Johnson, E. H. Oelkers, and H. C. Helgeson, "SUPCRT92: A Software Package for Calculating the Standard Molal Thermodynamic Properties of Minerals, Gases, Aqueous Species, and Reactions from 1 to

5000 Bars and 0 to 1000°C," Comp. Geosci. **18**, 899–947 (1992).

27. I. N. Kigai, "A Model of Multistage Ore Formation Consistent with Variations of Main Hydrothermal Process Parameters," in *Main Parameters of Natural Processes of Endogenic Ore Formation* (Nauka, Novosibirsk, 1979), Vol. 2, pp. 7–34 [in Russian].
28. A. I. Krivtsov, I. F. Migachev, and V. S. Popov, *Porphyry Copper Deposits of the World* (Nedra, Moscow, 1986) [in Russian].
29. A. I. Krivtsov, V. S. Zvezdov, I. F. Migachev, and O. V. Minina, *Porphyry Copper Deposits* (TsNIGRI, Moscow, 2001) [in Russian].
30. S. G. Kryazhev, Yu. V. Vasyuta, and M. K. Kharrasov, "Technique of Bulk Chemical Analysis of Inclusions in Quartz," in *Proceedings of XI International Conference on Thermobarogeochemistry* (VNIISIMS, Aleksandrov, 2003), pp. 6–10 [in Russian].
31. T. K. Kyzer, "Stable Isotope Geochemistry of Low Temperature Fluids," Mineral. Assoc. Canad. Short Course **13**, 287–336 (1987).
32. J. R. Lang, Y. Guan, and C. J. Eastoe, "Stable Isotope Studies of Sulfates and Sulfides in the Mineral Park Porphyry Cu–Mo System, Arizona," Econ. Geol. **84**, 650–662 (1989).
33. D. J. Lowell and J. M. Guilbert, "Lateral and Vertical Alteration-Mineralization Zoning in Porphyry Ore Deposits," Econ. Geol. **65** (4), 373–408 (1970).
34. Yu. V. Lyakhov, N. N. Pavlun, A. V. Piznyur, et al., *Thermobarogeochemistry of Gold (Forecasting, Exploration, and Evaluation of Ore Mineralization)* (Svit, Lvov, 1995) [in Russian].
35. J. T. Nash, *Fluid-Inclusion Petrology: Data from Porphyry Copper Deposits and Applications to Explorations* (US Govern. Printing Office, Washington, DC, 1976).
36. I. Ya. Nekrasov, *Geochemistry, Mineralogy, and Genesis of Gold Deposits* (Nauka, Moscow, 1991) [in Russian].
37. V. S. Popov, *Geology and Genesis of Porphyry Copper and Molybdenum Deposits* (Nauka, Moscow, 1977) [in Russian].
38. V. Yu. Prokof'ev and L. D. Zorina, "Evolution of Fluids in the Darasun Ore–Magmatic System (Eastern Transbaikal Region)," Dokl. Akad. Nauk **335** (2), 206–209 (1994).
39. V. Yu. Prokof'ev and L. D. Zorina, "Fluid Regime of the Darasun Ore–Magmatic System (Eastern Transbaikal Region): Evidence from Fluid Inclusions," Geol. Geofiz. **37** (5), 50–61 (1996).
40. V. Yu. Prokof'ev, A. M. Spiridonov, T. M. Kuz'mina, et al., "Specific Physicochemical Features of Ore Formation at the Kariisky Gold Deposit, Eastern Transbaikal Region)," Geokhimiya **35** (4), 423–434 (1997) [Geochem. Int. **35** (4), 368–378 (1997)].
41. V. Yu. Prokof'ev, N. S. Bortnikov, L. D. Zorina, et al., "Specific Genetic Features of the Darasun Gold–Sulfide Deposit (Eastern Transbaikal Region)," Geol. Rudn. Mestorozhd. **42** (6), 526–548 (2000) [Geol. Ore Deposits **42** (6), 474–495 (2000)].
42. V. Yu. Prokof'ev, A. N. Krasnov, V. A. Kovalenker, and N. V. Trubkin, "Mineral Microinclusions in Pyrite of the Talatui Gold Deposit (Eastern Transbaikal Region)," in *Proceedings of the Annual Session of the Moscow Division of Russ. Mineral. Society* (IGEM, Moscow, 2005a), p. 114 [in Russian].
43. V. Yu. Prokof'ev, L. D. Zorina, V. A. Kovalenker, and G. F. Il'ina, "First Data on the Origin of the Talatui Gold Deposit (Eastern Transbaikal Region)," Dokl. Akad. Nauk **401** (2), 221–225 (2005b) [Dokl. Earth Sci. **401** (2), 315–318 (2005b)].
44. V. Yu. Prokof'ev, I. A. Baksheev, L. D. Zorina, et al., "First Estimation of Ore Gold Age at the Darasun Deposit (Eastern Transbaikal Region) with Sm–Nd Method," Dokl. Akad. Nauk **409** (5), 673–676 (2006) [Dokl. Earth Sci. **409A** (6), 963–966 (2006)].
45. E. Roedder, "Fluid Inclusion Studies on the Porphyry-Type Ore Deposits at Bingham, Utah, Butte, Montana, and Climax, Colorado," Econ. Geol. **66**, 98–120 (1971).
46. G. Ruggieri, P. Lattanzi, S. S. Luxoro, et al., "Geology, Mineralogy, and Fluid Inclusion Data of the Furtei High-Sulfidation Gold Deposit, Sardinia, Italy," Econ. Geol. **92** (1), 1–19 (1997).
47. Yu. G. Safonov, "Hydrothermal Gold Deposits: Abundance, Geological–Genetic Types, and Productivity of Ore-Forming Systems," Geol. Rudn. Mestorozhd. **39** (1), 25–40 (1997) [Geol. Ore Deposits **39** (1), 20–32 (1997)].
48. Yu. G. Saitov, Yu. F. Kharitonov, and G. A. Shevchuk, "Mineral Resources of the Chita Oblast. Outlooks of Development and Further Expansion," Miner. Resursy Ross. Ekonom. Upravl., No. 4, 21–33 (2002).
49. S. M. F. Sheppard, "Characterization and Isotopic Variations in Natural Waters," Rev. Mineral. **16**, 165–183 (1986).
50. E. L. Shock, D. C. Sassani, M. Willis, and D. A. Sverjensky, "Inorganic Species in Geologic Fluids: Correlation among Standard Molar Thermodynamic Properties of Aqueous Ions and Hydroxide Complexes," Geochim. Cosmochim. Acta **61** (5), 907–950 (1997).
51. R. H. Sillitoe, "A Plate Tectonic Model for the Origin of Porphyry Copper Deposits," Econ. Geol. **67** (2), 184–197 (1972).
52. R. H. Sillitoe, "Gold-Rich Porphyry Deposits: Descriptive and Genetic Models and Their Role in Exploration and Discovery," in *Gold in 2000* (SEG Reviews), Vol. 13, pp. 315–345.
53. V. I. Sotnikov, V. A. Ponomarchuk, A. A. Sorokin, et al., "Age Boundaries of the Formation of Porphyry Cu–Mo Deposit Formation in the Framework of the Mongol–Okhotsk Orogenic Belt," Dokl. Akad. Nauk **403** (4), 522–525 (2005) [Dokl. Earth Sci. **403A** (6), 905–908 (2005)].
54. Yu. M. Stolyarov, "Anhydrite Microinclusions in Sulfide Ores," Izv. Akad. Nauk, Ser. Geol., No. 10, 138–147 (1992).
55. D. A. Sverjensky, E. L. Shock, and H. C. Helgeson, "Prediction of the Thermodynamic Properties of Aqueous Metal Complexes to 1000°C and 5 Kb," Geochim. Cosmochim. Acta **61**, 1359–1412 (1997).
56. D. A. Timofeevsky, *Geology and Mineralogy at the Darasun Gold Region* (Nedra, Moscow, 1972) [in Russian].
57. S. R. Titley and R. E. Bean, "Porphyry Copper Deposits," in *Econ. Geol. Seventy-Fifth Anniversary Volume*

(Econ. Geol. Publ. Company, 1981; Mir, Moscow, 1984), Vol. 1, pp. 245–333.

58. V. I. Ustinov, "Methodical Aspects of Geochemistry of Light Element Isotopes," in *Proceedings of All-Union Workshop on Isotope Geochemistry Methods* (GEOKhI, Moscow, 1983), pp. 7–8 [in Russian].
59. V. I. Ustinov and V. P. Strizhov, "Extraction of CO_2 from Carbonate-Bearing Rocks for Mass-Spectrometric Analysis," in *Proceedings of VI All-Union Symposium on Stable Isotopes in Geochemistry* (GEOKhI, Moscow, 1976), pp. 15–16 [in Russian].
60. G. V. Voitkevich, A. V. Kokin, A. E. Miroshnikov, and V. G. Prokhorov, *Handbook of Geochemistry* (Nedra, Moscow, 1990) [in Russian].
61. A. E. Vorob'ev and A. D. Gladush, *Geochemistry of Gold* (RUDN, Moscow, 2000) [in Russian].
62. T. Wagner and N. J. Cook, "Carrollite and Related Minerals of the Linnaeite Group: Solid Solutions and Nomenclature in the Light of New Data from the Siegerland District, Germany," Can. Mineral. **37** (3), 545–558 (1999).
63. Y. Wang, M. Sasaki, M. Sasada, and C-H. Chen, "Fluid Inclusion Studies of the Chinkuashih High-Sulfidation Gold–Copper Deposits in Taiwan," Chem. Geol. **154**, 155–167 (1999).
64. D. E. White, L. J. P. Muffler, and A. H. Truesdell, "Vapor-Dominated Hydrothermal Systems Compared with Hot-Water Systems," Econ. Geol. **66** (1), 75–97 (1971).
65. G. A. Yurgenson and T. N. Yurgenson, "The Darasun Ore Field," in *Deposits of Transbaikal Region* (Chita, 1995), Book II, pp. 3–18 [in Russian].
66. Yu. A. Zorin, L. D. Zorina, A. M. Spiridonov, and I. G. Rutshtein, "Geodynamic Setting of Gold Deposits in Eastern and Central Trans-Baikal (Chita Region, Russia)," Ore Geol. Rev. **17**, 215–232 (2001).